Rapid 3D-STORM imaging of diverse molecular targets in tissue

Running title: Nanoscale neuron imaging with RAIN-STORM

Authors: Nicholas E. Albrecht[1,2], Danye Jiang[1,2], Robert Hobson[4], Colenso M. Speer[5], Melanie A. Samuel[1,2,‡]

Affiliations:
[1] Department of Neuroscience, Baylor College of Medicine, Houston, TX 77030
[2] Huffington Center on Aging, Baylor College of Medicine, Houston, TX 77030
[4] Bruker Nano Surfaces Division, Salt Lake City, UT 84108
[5] Department of Biology, University of Maryland, College Park, MD 20742

[‡] To whom correspondence should be addressed. Email: msamuel@bcm.edu

Number of pages: 37

Numbers of figures: 4

Number of supplemental tables: 2

Number of extended data figures: 5

Number of videos: 5

Competing Financial Interests. N.E.A, D.J., C.M.S., and M.A.S declare no competing financial interests. R.H. is an employee of Bruker Nano Surfaces.

Abstract

The precise organization of fine scale molecular architecture is critical for the nervous system and other biological functions and would benefit from nanoscopic imaging methods with improved accessibility, throughput, and native tissue compatibility. Here, we report RAIN-STORM, a rapid and scalable imaging approach that enables three-dimensional nanoscale target visualization for multiple subcellular and intracellular targets within tissue at depth. RAIN-STORM utilizes conventional tissue samples, readily available reagents in optimized formulas, requires no specialized sample handling, and is suitable for commercial instrumentation. To illustrate RAIN-STORM's ability for quantitative high-resolution nanoscopic tissue imaging, we utilized the well-organized but structurally complex retina. We show that RAIN-STORM is rapid and versatile, enabling 3D nanoscopic imaging of over 20 distinct targets to reveal known and novel nanoscale features of synapses, neurons, glia, and vascular. Further, imaging parameters are compatible with a wide range of tissue sources and molecular targets across a spectrum of biological structures. Finally, we show that this method can be applied to clinically derived samples and reveal the nanoscale distribution of molecular targets within human samples. RAIN-STORM thus enables rapid 3D imaging for a range of molecules, paving the way for high throughput studies of nanoscopic molecular features in intact tissue from diverse sources.

Introduction

The advent of single-molecule localization microscopy (SMLM) techniques have greatly increased the ability to resolve the location, density, and nanoscale spatial relationships of diverse molecules (Bates et al., 2007). Yet, largescale adoption of these techniques for tissue analysis remains limited, in part because most SMLM approaches are challenging to apply to thick samples where aberrations and background can limit imaging. As a result, most analysis of tissue molecular architecture continues to rely on immunofluorescence microscopy, immunoelectron microscopy, and fluorescent protein reporters. These powerful tools have shown that cellular and tissue function intimately depends on small-scale arrangements of proteins and cells, but how nanoscale biological structures are organized, and their relative molecular composition, remain unknown for most targets, cell types, and tissue sources.

To help address this challenge a number of bespoke SMLM solutions have been developed. These include in-house, specialized microcopy and optical systems, customized analysis software, and advanced sample preparation techniques. For example, cultured cells have been visualized in three-dimensional volumes using astigmatism (Huang et al., 2008), biplane imaging (Juette et al., 2008), an engineered point spread function (Pavani et al., 2009), and 4pi-imaging (Bewersdorf et al., 2006) , while tissue has been visualized using adaptive optics (Mlodzianoski et al., 2018), biplane imaging (Bewersdorf et al., 2006), self-interfering point spread functions (Bon et al., 2018), light-sheet approaches (Greiss et al., 2016), and ultrathin physical sample sectioning (Sigal et al., 2015). While these methods have greatly advanced 3D SMLM capability in the field and led to numerous discoveries (Bowler et al., 2019; Chamma et

al., 2016; Leterrier et al., 2015; Sigal et al., 2015; Suleiman et al., 2013; van den Dries et al., 2013), significant challenges remain. The first is accessibility. Most 3D SMLM approaches rely on techniques, systems, and expertise that are available only to a handful of specialists. The second is simplicity and throughput. For instance, one useful approach called serial-section STORM uses ultrathin sectioning and reconstruction, but the labor and imaging time for this technique make it best suited for deep imaging of small sample numbers. The third is target compatibility within native tissue environments. Most current methods report imaging capabilities using only a small number of antibodies (Mikhaylova et al., 2015; Mönkemöller et al., 2015), and approaches such as expansion microscopy are not always suitable for low density targets (Chen et al., 2015; Ku et al., 2016; Tillberg et al., 2016).

We set out to develop a new imaging method that would complement and combine the strengths of currently available methods for nanoscopic tissue imaging in general and for neural circuits specifically. Our criteria for this method were to improve the accessibility, throughput, and compatibility of 3D nanoscopic tissue imaging so that it can be broadly and readily applied to diverse tissue sources and target types. Toward this goal, we present Rapid Imaging of tissues at the Nanoscale (RAIN-STORM), a method for utilizing standard tissue samples to generate SMLM data at depth for a wide range of molecular targets using commercially available reagents and imaging systems. To achieve this goal, we optimized labeling and imaging conditions from 125 distinct tested parameters for over 20 molecular targets in murine tissue and validated methods in four additional species. We show that RAIN-STORM is rapid and versatile, enabling 3D nanoscopic imaging with a 24-hour turnaround. Further, these imaging parameters

are compatible with a wide range of tissue sources and a large number of molecular targets across a spectrum of biological structures. Finally, we show that this method can be applied to clinically derived samples and reveal the nanoscale distribution of molecular targets within human samples. RAIN-STORM thus enables rapid 3D STORM for a range of molecules, paving the way for high throughput studies of nanoscopic molecular features in intact tissue from diverse sources.

Results

A central criterion for our method is compatibility with standard tissue preparation protocols that require little special tissue handling. To test this, we used the mouse retina because it has a highly defined laminar structure that provides endogenous fiduciaries for evaluating the labeling precision of multiple molecular targets (Sanes & Zipursky, 2010). To begin, retinas were harvested from wildtype adult mice and processed with a standard tissue preparation protocol (Albrecht et al., 2018) that involves a short primary fixation, cryoprotection, embedding in tissue freezing medium, sectioning at 10 µm on a cryostat, and mounting on coated glass slides (**Figure 1a**). Using this basic framework, we tested and adapted variations for each preparatory step to find ideal conditions suitable for SMLM-based imaging. Sample preparation thus does not require labor-intensive handling, and results in staining ready slides within hours of tissue harvest. For turnkey nanoscopic imaging, we utilized a commercial SMLM imaging system, the Vutara 352 (Bruker, Billerica MA), together with associated commercial image analysis software. This system enables multicolor STORM imaging

within a 40μm-by-40μm planar region of interest and achieves single molecule imaging of individual emitters by recording the point spread function (PSF) in two imaging planes simultaneously (**Figure 1 – figure supplement 1**). Single-molecule localization in 3D is based on calibration data generated from fiducial imaging.

We selected the calcium buffering protein Calbindin (Calb1) and the synapse protein PSD95 (Postsynaptic density protein 95, also known as Dlg4) to optimize our labeling and imaging parameters. Since Calbindin specifically and densely fills the cell body and neurite terminals of retina horizontal neurons (Celio, 1990; Uesugi et al., 1992), while PSD95 moderately labels synapses (Hunt et al., 1996; Koulen et al., 1998), we reasoned that optimizing our imaging processes around these targets would enable us to evaluate the efficacy of our method across a range of cell structures and protein densities. Moreover, because Calbindin and PSD95 are found in other central nervous system regions (Celio, 1990; Hunt et al., 1996) preparation methods compatible with these targets may extend to other tissue types.

Significant image aberration and background in STORM tissue imaging can result from suboptimal sample preparation, imaging buffer, and image acquisition conditions. We reasoned that tuning these parameters for 3D STORM imaging could markedly improve nanoscale image quality. We focused on the following features: preservation of tissue structure, epitope integrity, reduced background fluorescence, high labeling specificity, uniform antibody penetration, and increased localization density within samples. We performed STORM imaging following precise manipulation of 80 fixation and staining variations and 45 buffer conditions, resulting in a total of 125 test conditions (**Figure 1b**, **Supplemental Table 1**, and **Figure 1 – figure supplement 2**).

We chose the best performing conditions based on the following criteria: 1) The total number of localizations acquired (**Figure 1d**), 2) epitope and morphological detail preservation, 3) the relative background level (noise) observed as isolated localizations or spurious antibody signal (**Figure 1e**), and 4) the calculated resolution across planar (XY, **Figure 1f**) and axial (XZ, **Figure 1g**) image dimensions using Fourier Ring Correlation (FRC) metrics (Nieuwenhuizen et al., 2013). Samples were obtained from three independently prepared animals, giving three independent measurements per condition tested. Within this parameter space, we first investigated the effects of primary fixation on tissue quality and imaging. We found that autofluorescence could generally be lowered by reducing fixative concentrations, and that temperature played an important role in limiting structural distortions and preserving epitopes. A cold fixation (4ºC) at a relatively low concentration of paraformaldehyde (2% PFA) yielded the best labeling density and imaging metrics (**Supplemental Table 1** and **Figure 1 – figure supplement 2**). Second, we tested diverse fixation quenching reagents, staining buffer components, primary and secondary antibody concentrations, and both post-fixation and post-fixation quenching methods. Of these, we found that variations in post-fixation and fixation quenching conditions had the largest effects on tissue integrity and final image quality (e.g., 47.6 ± 2.8 nm for those with post-fixation versus 72.8 ± 3.0 nm for those without, **Supplemental Table 1**). Image resolution was further increased, and background fluorescence decreased, by quenching in 100mM NH_4Cl for 30min (50.5 ± 2.1 nm for treated versus 72.8 ± 3.0 nm for untreated samples, **Supplemental Table 1**)

We then tested multiple dilutions for a range of primary and secondary antibodies to identify the concentrations that resulted in the highest signal-to-noise ratio.

(**Supplemental Table 1**). We found that many of our targets benefitted from using increased primary and secondary antibody concentrations relative to standard histological preparations (e.g., anti-Calbindin primary antibody is optimal at 1.0 ug/ml in STORM compared to 0.1 ug/ml in diffraction-limited microscopy). For secondary antibodies, we found a significant difference between conditions, with high concentrations (5.0 µg/ml) providing increased labeling density relative to standard confocal dilutions (0.5 µg/ml, ~$12.4x10^6$ vs. ~$7.2x10^6$, localizations respectively) though both were sufficient to image primary-labeled structures for all tested fluorophores (**Supplemental Table 1**).

Finally, we undertook a thorough examination of imaging buffer conditions and tested the effects of 1) oxygen-scavenging enzymes, 2) catalase concentration, 3) the ratio of thiols [ß-mercaptoethanol (BME) versus ethanolamine (MEA)], and 4) triplet-state quenching [cyclooctatetraene (COT)]. Results from these tests are summarized in **Supplemental Table 1**. For example, we found that the use of pyranose oxidase was preferable to glucose oxidase as it provided a more stable and longer-lived imaging environment. In addition, we determined that the addition of 2mM COT led to an increase in the total number of localizations across both channels (**Supplemental Table 1** and **Figure 1 – figure supplement 2**). The final sample preparation and imaging method was chosen from all tested parameters using the best performing parameters from each optimization step. This selection considered whether balanced data acquisition and quality could be achieved, the total number of localizations acquired, and the absolute image resolution for each fluorophore. Our final preparation and imaging method is termed RAIN-STORM and is comprised of readily accessible

reagents and six simple steps that include a moderate initial fixation (2% PFA for one hour at 4ºC), quenching of autofluorescence (100 mM Glycine for one hour at 4ºC), primary and secondary staining using a serum-based blocking and permeabilization buffer (5% serum, 0.3% Triton-X100), post-fixation (4% PFA for 30 min at 4ºC), and a final round of quenching (100 mM NH_4Cl for 30min, **Figure 1b**).

To illustrate RAIN-STORM's ability we reconstructed horizontal cells in 3D. We found our methods markedly improved quantitative resolution of nanoscopic cellular features (**Figure 1 h-i**). For example, we were able to observe distinct neurites of diverse morphologies arising from the cell body, which terminated in a high number of postsynaptic invaginations. These synaptic terminals were easily resolved and structurally separated from their neighbors, demonstrating markedly improved spatial resolution (31.2 ± 0.4nm and 61.1 ± 2.9nm for Calbindin labeled with CF568 and AF647, respectively, compared to ~200-250nm resolution for typical confocal microscopy). RAIN-STORM also provides improved resolution at along the Z axis at depth, suggesting it is well suited for 3D super-resolution imaging of molecular targets within tissue volumes. To assess this, we computed the resolution of RAIN-STORM as a function of image depth at discrete imaging planes throughout the image volume. As expected, we found that planar resolution was improved closer to the objective relative to further away (30.0 ±1.5nm versus 42.3 ± 4.8nm**, Figure 1 – figure supplement 3**). To accommodate biological variability and nonhomogeneous structures, we report the aggregate resolution across the entire 10μm image stack. We achieve a Z-axis resolution of 42.2 ± 1.2nm and 79.3 ± 0.3nm for CF568 and AF647, respectively. RAIN-STORM thus offers the advantage of improved spatial resolution and can be used to

visualize nanoscopic neural structures in large-field 3D volumes across the imaging plane to reconstruct all processes arising from a single cell (**Figure 1, Video 1**).

RAIN-STORM is also versatile, enabling nanoscopic imaging of a diverse array of molecular targets. To assess this, we took advantage of the wide spectrum of specific antibody markers available in the retina (Sanes & Zipursky, 2010) and tested the robustness of this approach across 22 validated molecular targets (**Supplemental Table 2, Figure 2** and **Figure 2 – figure supplement 1**). These included diverse cell structures, types, and molecular targets, such as synapse proteins (Bassoon, Bsn; RIBEYE, Ctbp2; Connexin 43, Gja1; Dystrophin, Dmd; Piccolo, Pclo; PSD95, Dlg4), vasculature markers (CD31, Pcam1; Collagen IV, Col4A1; Desmin, Des; CSPG4, Cspg4), glia (Iba1, Aif1; GFAP, Gfap; GS, Glul), excitatory interneurons (PKCα, Prkca; SCGN, Scgn), presynaptic photoreceptors (CAR, Arr3), and intracellular proteins and structures (Tau, Mapt; Tomm20, mitochondria, **Figure 2** and **Figure 2 – figure supplement 2**). We found that approximately 90% of the commercially available antibodies tested were compatible with RAIN-STORM and could be used to successfully obtain SMLM images of individual targets at depth within intact tissue slices (**Figure 2, Videos 1-3**). Further, in all cases labeling of the proper cell type or structure at the proper location was observed (**Figure 2 – Figure Supplement 1 and 2**). In addition, our results resolve novel nanoscale structural features and molecular distributions. For example, we observed that astrocyte end feet form fine (~100-200nm) filamentous structures and what appears to be a mesh of fibers interdigitating the ganglion cell layer (**Video 3**). We also resolved individual dystrophin puncta in the outer retina synapse layer, which are thought to interact with actin filaments to enable contact

formation between photoreceptors and ON-bipolar cells (Schmitz & Drenckhahn, 1997) (**Figure 2a**). Finally, we observed vascular associated interpericyte tunneling nanotubes (IP-TNTs, **Figure 2b**, **Video 2**). These ~500nm diameter structures enable pericyte driven neurovascular coupling (Alarcon-Martinez et al., 2020) but their molecular composition is largely unknown. We show that Collagen IV comprises the core of these tubes, forming a solid filament connecting two hollow blood vessels (**Video 2**). These results suggest that RAIN-STORM is effective to image many targets, resolves biologically relevant protein localization, and can be used to discover unknown nanoscopic cellular structures with high fidelity.

Multicolor RAIN-STORM imaging is also robust across both multiple intracellular targets and in tissue from diverse species (**Figure 3**). We observed robust imaging with multiple target combinations. These include a neuron subtype marker together with synapse antibodies, staining for two distinct post-synaptic neuron types, as well as co-staining for vascular markers and astrocytes (**Figure 3a-c**). Using these combinations, we were able to resolve contact sites, overlapping and non-overlapping cellular structures, and fine cellular interactions. For example, astrocytes and blood vessel co-staining revealed fine astrocytic filaments enshrouding and forming close contacts with neighboring vessels (**Figure 3b**). Further, RAIN-STORM imaging was compatible with tissue from diverse species, revealing both conserved and unique nanoscopic features across mouse, rabbit, macaque, and pig tissues (**Figure 3d-i**). For instance, co-staining for rod bipolar cells and their synapses (PKCα and PSD95, respectively) in adult macaque, rabbit, and pig retina showed that despite similar functions and molecular identities, rod bipolar cells have incredibly diverse dendritic structures (**Figure 3d-f**).

Rabbit rod bipolar cell bodies were rounder and less elongated relative to pig, macaque, and mouse, with arbors that branched closer to the cell body. Notably, PSD95 labeling was confined to the outer layer of rod bipolar dendrites across species, suggesting presynaptic contacts are restricted to this region independent of species type. These data indicate that RAIN-STORM is suitable for 3D multicolor imaging in tissue from a range of species to simultaneously visualize diverse molecular targets.

RAIN-STORM can also be used to visualize, quantify, and measure features of small structures, including synapses. To assess this, we imaged retina ribbon synapses in the outer plexiform layer **(Figure 4a**). This region has two advantages. First, the architecture and composition of outer retina synapses have been well-characterized, allowing validation of our method. Second, because each photoreceptor forms connections at one distal location, the relationship between the structure and of both pre- and postsynaptic neurons relative to their connectivity can be directly examined. To resolve both murine ribbon synapses and their postsynaptic partners, we applied antibodies against the synapse scaffolding protein RIBEYE (Moser et al., 2020) together with the postsynaptic bipolar marker PKCα (**Figure 4a-c**) and used CF568- and AlexaFluor647 (AF647)-conjugated secondary antibodies to serially visualize both targets. We reconstructed individual RIBEYE labeled ribbons and assessed their shape, 2D-projected length, and 2D-projected area. RIBEYE showed a rich variety of ribbon morphologies, including many that appeared in a horseshoe shape and others that appear flatter, consistent with the more elongated contacts of basally located rods (Li et al., 2016) Measurements taken of individual ribbons (n = 844) across four adult mice showed an average ribbon length of 1.92 ± 0.30μm and a 2D projected area of 0.52 ±

0.13 μm^2 **(Figure 4d-f** and **Video 4)**. Notably, these values are comparable to those obtained using Structured Illumination Microscopy (Dembla et al., 2020) (SIM, 1.25 ± 0.05 μm to 1.95 ± 0.07 μm in length), validating the specificity and accuracy of RAIN-STORM for measuring cellular structures. Together, these data suggest that RAIN-STORM can be used to reconstruct and measure defined neuron and synapse types at nanoscale resolution within tissue.

Finally, we found that RAIN-STORM is compatible with human tissue. Ribbon synapses are also present in the human outer retina (Moser et al., 2020), but their relative size and organization have not been well mapped. Eyes from two adult human donors (aged 40 and 58 years) were processed for RAIN-STORM with similar parameters to those in mouse and stained with antibodies against RIBEYE and PKCα. As above, images were acquired using sequential imaging for each of the two channels. Reconstruction and quantification of human RIBEYE-labeled synapses showed an average length of 1.81 ± 0.03μm, which is similar in size to mouse ribbon synapses. Human ribbons also displayed a similar variety in shape and morphology as those found in mouse (**Figure 3g-i, Video 5**). Of note, we did observe fewer synapses in the human samples relative to the mouse, although this may be due to the inherent delay in human post-mortem sample collection rather than a biologically relevant difference.

Discussion

In this paper we introduce RAIN-STORM, a rapid and scalable imaging approach that enables 3D nanoscale target visualization for multiple subcellular and intracellular targets within tissue at depth. We took advantage of the well-organized but structurally

299 complex retina circuit to demonstrate that RAIN-STORM can resolve nanoscale
300 features for a wide range of cell types and structures. This enabled us to validate known
301 nanoscale structures as well as map novel cellular features of neurons, glia, and the
302 vasculature. In addition, we visualized and quantified hundreds of single human and
303 mouse synapses across multiple individuals. The acquisition of this dataset was
304 facilitated by the high throughput nature of RAIN-STORM, and we show that this
305 method is practical for analyzing specimens from multiple samples and species. Finally,
306 because RAIN-STORM was developed to be compatible with a commercial imaging
307 system and standard tissue processing, it is open to a range of researchers,
308 applications, and clinical samples.

309 RAIN-STORM offers a number of advantages relative to existing 3D SMLM
310 methods, including its experimental accessibility. We maximized its availability by using
311 a user-friendly commercial imaging system so that this method could be readily adopted
312 by the wider scientific community. With these advances, 3D tissue RAIN-STORM
313 imaging has the capacity to be as routine as confocal imaging in many laboratories. In
314 contrast, other 3D STORM imaging approaches, while excellent (Huang et al., 2008;
315 Nehme et al., 2020; Punge et al., 2008; Xu et al., 2015), rely on custom built
316 microscopes and require optics expertise and resources that are largely unavailable to
317 most researchers. Also of note, the optimal $R_{X;Z}$ resolution achieved with RAIN-STORM
318 ($R_{X;Z}$ = 61.1±2.9; 79.3±0.3) approaches, and in some cases exceeds, that of bespoke
319 systems (e.g. SELFI, $R_{X;Z}$ = 68±20; 115±32nm). RAIN-STORM is also rapid. We
320 developed our method for use with conventionally prepared tissue samples, requiring
321 only standard reagents and tools. Unlike serial array tomography EM (Micheva & Smith,

2007), serial section SMLM (Nanguneri et al., 2012) or related (Li et al., 2016) approaches, RAIN-STORM does not require time intensive ultrathin sectioning, successive section imaging, alignment, or reconstruction. Due to the straightforward nature of sample preparation and the relatively large field of view of our system, extensive datasets can be acquired quickly. For instance, in our study of human and mouse outer retina synapses, each dataset consisted of hundreds of synapses and was acquired with a 24-hour turnaround from sample collection to image ready tissue, followed by approximately 8 hours of imaging time per species. RAIN-STORM is thus uniquely suitable for large sample numbers and the acquisition and quantitative analysis of extensive datasets

While improvements in accessibility, speed, and target compatibility were major motivations for the development of RAIN-STORM, several optimized parameters were uncovered that could be useful in other nanoscopic imaging applications. Toward this end, we report quantitative imaging metrics for all 125 tested parameters as a resource for the community. Among these, some unexpected advantages of various conditions were discovered. For example, including a post-fixation step once primary and secondary antibody staining had been performed improved resolution by ~20nm. We also found that the ratio of BME to MEA could be used to tune fluorophore switching properties, and that BME (140 mM) combined with MEA (40 mM) was most suitable to induce balanced blinking of fluorophores in both imaging channels. Given these results, we anticipate that many of the parameters that we report will be useful to other SMLM approaches.

RAIN-STORM also offers new opportunities for the discovery of novel nanoscopic structures or molecular components. A diverse array of targets could be readily visualized across a range of cell types and subcellular structures, with ~90% of tested commercial antibodies showing good labeling and resolution. By comparison, most current 3D STORM methods have been developed using a handful of molecular targets (<5), many of which are cytoskeletal (Chamma et al., 2016; Mikhaylova et al., 2015; Mönkemöller et al., 2015; Stahley et al., 2016; van den Dries et al., 2013). RAIN-STORM is thus suitable for biologic discovery of new nanoscopic structures or mapping the distribution or localization of a diverse array of molecular components.

RAIN-STORM may also be useful for the study of molecules and structures beyond those described here. As with other SMLM methods, the relative density of a given protein and the specificity of available antibodies are key factors in determining good targets for RAIN-STORM. As expected, the relative density of an individual target influences the degree of structural filling. Because single molecules are visualized with this approach, the relative labeling density of a given target can report on the location and area of individual substructures, as we demonstrated for ribbon synapses. For imaging the shape and structure of individual cell types, the relative density of a given protein and the availability of high-quality antibodies can make some targets more useful than others. For example, PKCα densely and specifically labels rod bipolar cells and reliably reveals the entirety of the bipolar cellular architecture at the nanoscale, while Iba1, a microglia marker, appears less dense and fills microglia structures incompletely. Notably, RAIN-STORM parameters performed consistently well across molecular targets and species, suggesting RAIN-STORM methods should provide a

good baseline for imaging of additional molecular targets and tissue types not tested here.

The many technical advantages of RAIN-STORM enable access to important aspects of glia and neural circuit molecular architecture that were previously difficult to visualize and measure within tissue. For instance, RAIN-STORM provides easy and rapid quantification of individual PSD95 and Ribeye labeled synapses in 3D volumes of neuropil in both mouse and human clinical specimens. Using this approach, we were also able to validate the existence of IP-TNTs and map new molecular features of these structures. This includes the presence of a what appears to be a solid collagen IV core filament that may provide stability to these small structures. Future studies will shed light on how this collagen filament resides within the nanotube and whether it participates in IP-TNT-mediated neurovascular coupling (Alarcon-Martinez et al., 2020). In addition, we documented ~100-200nm filaments arising from astrocytes in the ganglion cell layer. Various roles for retinal astrocytes have been described, including vascular patterning (O'Sullivan et al., 2017; Tao & Zhang, 2016), but our data hint that they may also physically interact with and perhaps modulate adult retinal neurons through nanoscale structural interactions (Arizono et al., 2020). Given that changes in the numbers and densities of synapses, neurovascular coupling, and in neuron-glia interactions are thought to be central to many neurological and cognitive disorders (Lian and Zheng, 2016; Kempuraj et al., 2018; Verdugo et al., 2019), the potential of rigorously and rapidly measuring such features is an important advance. In addition, because RAIN-STORM is readily compatible with human tissue, this method will also be useful for clinical specimens and comparisons between human disease and animal

models. Finally, since RAIN-STORM can be leveraged together with genetic reporters and viral labeling strategies to obtain directed co-imaging of various targets, these methods may offer additional combinatorial advances for overlaying molecular information on cellular ultrastructure. Such investigations of neural circuits and other tissues will help continue to drive discovery of novel nanoscale biological features in native tissue environments in healthy and diseased states.

Materials and Methods

Coverslip Preparation

Small batches of #1.5H 22mm round glass coverslips (Neuvitro #GG-25-1.5H) were cleaned via sonication. Coverslips were then submerged in 5M sodium hydroxide (Fisher Scientific #1310-73-2) for 30 minutes and serially washed three times in deionized water. Coverslips were next washed in serial dilutions of ethanol (70%, 90%, 100%) for 30 minutes each and then allowed to dry. Once dry, coverslips were dipped in a solution of 0.5% (m/v) Gelatin A, 7mM Chromium(III) Potassium Sulfate in PBS and again were allowed to dry again before storing up to one month at room temperature.

Experimental Model and Subject Details

For mouse tissue, retinas were collected from four 6 to 8-week-old C57BL/6J animals. Experiments were carried out in male and female mice in accordance with the recommendations in the Guide for the Care and Use of Laboratory Animals of the NIH under protocols approved by the BCM Institutional Animal Care and Use Committee.

Macaque (N = 2), rabbit (N =2), and pig (N = 3) retinal tissue were obtained via the Baylor College of Medicine Center for Comparative Medicine veterinary from unrelated surgical procedures. Human donor eyes (N = 2) were obtained in collaboration with the Lions Eye Bank of Texas at Baylor College of Medicine. Informed consent was acquired from all patients and/or participating family members in accordance with EBAA and FDA regulatory standards. Subjects were 40 and 58 years old and had no documented history of eye disease.

Tissue preparation

Details for tissue preparation and staining methods are provided for the optimized RAIN-STORM protocol. Tested variations on this protocol are listed in **Supplemental Table 1**. Briefly, tested parameters included both 25ºC and 4ºC fixations, PFA concentrations of 1%, 2%, and 4%, Glutaraldehyde preparations with PFA (2% PFA, 0.3% GA), or glutaraldehyde by itself (0.3% GA), each prepared in phosphate buffered saline (PBS), with fixation times of 30, 60, or 120 minutes. Quenching conditions included ammonium chloride (10mM, 100mM), glycine (10mM, 100mM) or sodium borohydride (0.1%, 0.5% w/v). For the final selected tissue preparation condition, mouse eyes were enucleated and placed in 2% paraformaldehyde for 1 hour at 4ºC, then subsequently rinsed in 100mM glycine solution for 1 hour at 4ºC. Samples were then washed in PBS for 30 minutes and stored in PBS. Eye cups were then dissected, removing the cornea and the lens. Samples were then allowed to fully equilibrate in 30% sucrose until the tissue sank (~45-60 minutes). Tissue was serially washed by hand in Optimal Cutting Temperature (OCT) compound to remove excess sucrose and

436 subsequently placed into molds filled (OCT) compound (Sakura, Torrance, CA).
437 Embedded tissue was then frozen using methyl butane chilled on dry ice. Human eyes
438 were prepared using our final selected fixation condition of 2% PFA at 4ºC but were
439 fixed for 4 hours given the increase in tissue thickness. All other conditions were
440 identical to those detailed above. All blocks were then stored at -80ºC until ready for
441 use. Tissue was sectioned at 10µm and mounted on prepared coverslips.
442
443
444 **Antibody Staining**
445 For quantification and final images, slides were incubated in the optimized blocking
446 solution (5% normal donkey serum and 0.3% Triton X-100 in PBS) for 1 hour and then
447 with primary antibodies diluted in blocking solution (Table 1) for a minimum of 12 hours
448 at 4ºC. Other tested conditions include variations in concentrations of Triton-X100
449 (0.1%, 0.3%, 0.5%, 1.0%, 2.0%), Saponin (0.1%, 0.3%, 0.5%, 1.0%, 2.0%), and Normal
450 Donkey Serum (1%, 3%, 5%, 10%, 15%). Samples were washed with PBS three times
451 for 20 minutes and then incubated with commercial dye- conjugated secondary
452 antibodies diluted in blocking solution (AF647-conjugates from Jackson
453 ImmunoResearch Laboratories, West Grove, PA, and CF568-conjugates from Biotium,
454 Fremont, CA) for 1 hour at room temperature. Slides were then washed with PBS three
455 times for 20 minutes prior to applying a 4% PFA solution as a postfix for 30 minutes.
456 Slides were washed with PBS three times for 20 minutes each, 100mM NH_4Cl was
457 applied for 30min, and slides were again washed with PBS three times for 20 minutes
458 each. Samples were stored in PBS until imaging.

459

460 **Imaging Buffer**

461 Imaging buffer for use in STORM was prepared using stock solutions of one of three
462 oxygen scavenging enzymes: pyranose oxidase (0.5 U/μL, Millipore Sigma #P4234-
463 250UN), glucose oxidase (Millipore Sigma #G2133-50KU), or protocatechurate 3,4-
464 dioxygenase (PCD, Millipore Sigma #P8279-25UN). Each oxygen-scavenging enzyme
465 was used to name the associated buffer formulation. Tested imaging buffers also
466 contained bovine-derived catalase (100 U/μL, Millipore Sigma #C1345-10G),
467 cysteamine hydrochloride (MEA, 1 M, Chem-Impex International #02839), and 2-
468 mercaptoethanol (BME, Millipore Sigma #M6250-250ML). When PCD was used, its
469 substrate protocatechuic acid (PCA, 3,4-dehydroxybenzoic acid, Millipore Sigma
470 #37580-25G-F) was also included. For a given buffer formulation, one of the
471 components was varied by concentration, keeping all others constant. Once this was
472 performed for each buffer-enzyme combination, the final selected buffer was tested with
473 either cyclooctatetraene (COT, Millipore Sigma #138924-1G) or trolox (Millipore Sigma
474 #238813-1G) in varied concentrations (1mM, 2mM, or 5mM). Stock solution aliquots
475 were kept frozen at -80ºC until just prior to use. Aliquots were thawed at room
476 temperature and added to a freshly prepared solution of 30% (m/v) glucose in PBS.
477 Once prepared, imaging buffer was allowed to equilibrate for 20 minutes and then used.

478

479 **Imaging and Image Processing**

480 Image acquisition was performed on a Bruker Vutara 352 (Bruker, Billerica, MA) using a
481 water objective (UPLSAPO60XW). Stained samples were mounted in a collared well

(Thermofisher Scientific #A7816), and 1mL of imaging buffer was added on top in an open well configuration. All images were acquired at 200nm axial steps using a framerate of 67 Hz for AF647 and 40Hz for CF568 across the full 10μm thickness of tissue using three sequential cycles of 250 frame-captures for each channel, yielding a total of 38250 frames per probe per sample. Between each cycle a timed pause was included to allow for the imaging buffer to re-equilibrate. 3D nanoscopic imaging volumes were thus 40μm by 40μm by 10μm (16,000 μm^3). For the 640nm, 561nm and 405nm excitation lasers, laser powers of ~98-110mW (6125-6875 W/cm^2), ~90-100mW (5625-6250 W/cm^2), and ~2-6mW (125-375 W/cm^2), were measured at the sample using a 40μm by 40μm field of view. Data were then clustered to determine associated and contiguous structures within the image using the Ordering Points to Identify the Clustering Structure (OPTICS) algorithm. To analyze images, a general particle distance of 0.16 μm and a particle count of 25 was used for all channels on all images. The particle distance refers to the maximum allowed distance that a particle can be from another particle in order to be included in a given cluster while the particle count reflects the minimum required number of particles required to form a cluster. Any non-clustered localizations were removed from the image. Once filtering and clustering were complete, an FRC analysis was performed to determine the global aggregate resolution of the sample in the XY and XZ dimensions for each target imaged using three repeat measurements for curve smoothing.

Data availability

All data are available on reasonable request from the authors.

505 **Figure 1: Nanoscale 3D imaging of neurons in tissue. a**, Schematic of the RAIN-
506 STORM workflow. Eyes are enucleated, and retina cups are dissected, fixed, and
507 quenched. Retinal cups are then cryopreserved and embedded in OCT prior to
508 sectioning and mounting onto prepared coverslips. Samples are stained with primary
509 and secondary antibodies, post-fixed and quenched, and finally mounted in open wells
510 containing imaging buffer. **b**, Schematic of tested parameters with the number of
511 variations tested for each category. **c**, Optimized RAIN-STORM parameters and
512 associated preparation timeline. **d-g**, Representative quantifications for six exemplar
513 tested parameters representing three different stages of sample preparation, staining,
514 and imaging. The total localizations acquired (**d**) impacts the final localization density,
515 while the total removal of non-structured localizations (**e**) measures the
516 noise/background for each condition. Calculated resolutions are also provided for the
517 XY-plane (**f**) and XZ-plane (**g**) for each condition using FRC. Among these conditions,
518 low levels of PFA and Trolox and moderate levels of normal donkey serum provided the
519 best image quality metrics and the least unwanted signal. **h**, Unoptimized STORM
520 image of a horizontal cell labeled with Calbindin. Putative synapses are indistinct with
521 little defining morphology or contiguous structure. **i**, RAIN-STORM image of a Calbindin-
522 labeled horizontal cell using optimized parameters demonstrates clear structural detail
523 across the neuronal arbor. Distinct synaptic terminals are visible together with the
524 connecting stalk arising from the neuron. N = 3 animals. Scale bars = 10 and 1 μm.
525 Data are represented as the mean ± the s.e.m.
526
527

Figure 2: RAIN-STORM delivers robust imaging for a diverse array of molecular targets. a, RAIN-STORM imaging of synaptic proteins PSD95, a marker for photoreceptor terminals, dystrophin, a synaptic structural protein in the outer plexiform layer, and RIBEYE, a scaffolding protein present in ribbon synapses. Individual synapse terminals can be observed with all three markers. **b**, RAIN-STORM imaging of vasculature proteins Collagen IV, a marker for blood vessels, Desmin, a filament protein that marks subsets of pericytes and vascular associated smooth muscle cells, and CSPG4, a pericyte marker. Vasculature associated interpericyte tunneling nanotubes are visible with both Collagen IV and CSPG4 (arrows). **c**, RAIN-STORM imaging of glial proteins GFAP, a marker for astrocytes, and GS, a marker for Müller glia. In each case, fine features of these cell types can be observed, including filament-like protrusions from astrocytes. **d**, RAIN-STORM imaging of excitatory neurons, SCGN, a marker for subsets of cone bipolar cells, and PKCα, a marker for rod bipolar cells. In each case, fine features of these images are representative of those acquired from N = 3 animals. Scale bars = 10 and 1 μm.

Figure 3: RAIN-STORM enables dual-channel super resolution imaging among diverse species.

a-c, RAIN-STORM imaging of two independent molecular target, including **(a)** cones (CAR, magenta, AF647) and synaptic terminals (PSD95, cyan, CF568), **(b)** vasculature (Collagen IVa, magenta, AF647) and astrocyte (GFAP, cyan, CF568) interactions, and **(c)** cone bipolar cells (SCGN, magenta, AF647) and rod bipolar cells (PKCα, cyan, CF568). **d-f**, RAIN-STORM imaging can be extended to diverse species. Retinas from

551 **(d)** macaque (N = 2 animals), **(e)** rabbit (N = 2 animals), and **(f)** pig (N = 3 animals)
552 were labeled with antibodies to rod bipolar cells (PKCα, magenta, AF647) and rod
553 photoreceptor terminals (PSD95, cyan, CF568). **g**, The total number of localizations that
554 were acquired pre- and post-processing for images in **d-f**. **h** are displayed together with
555 the XY planar resolutions of both AF647 (PKCα, magenta) and CF568 (PSD95, cyan).
556 Scale bars = 10 and 1 μm. Data are represented as the mean ± the s.e.m.
557
558 **Figure 4: RAIN-STORM quantifies structural and molecular features of synapses.**
559 **a**, Schematic of retina outer plexiform synapse organization. Rod photoreceptors
560 terminals (cyan) are presynaptic to invaginating post-synaptic horizontal cells (grey) and
561 bipolar cells (magenta). **b-c**, Diffraction-limited imaging of murine (**b**) and human (**c**)
562 retina outer plexiform synapses. Presynaptic photoreceptor terminals are labeled with
563 RIBEYE (cyan) while postsynaptic bipolar cells are labeled with PKCα (magenta). **d**,
564 Dual color RAIN-STORM imaging of murine rod bipolar cells (PKCα) and ribbon
565 synapses (RIBEYE) allows individual quantification of ribbons and shows a rich variety
566 of morphologies. **e-f**, Individual outer retina synapses (n = 844) were reconstructed from
567 adult mice (N = 4), and the largest 2D projected length (**e**, 1.92 ± 0.30 μm) and total
568 area (**f**, 0.52 ± 0.13 μm^2) were quantified for each synapse. **g**, RAIN-STORM imaging of
569 human rod bipolar cells (PKCα, magenta) and ribbon synapses (RIBEYE, cyan)
570 resolves interactions between pre- and postsynaptic neurons. **h-i**, Individual outer retina
571 synapses (n = 263) were reconstructed from human adult donors aged 40-58y (N = 2),
572 and the largest 2D projected length (**h**, 1.81 ± 0.03 μm) and total area (**i,** 0.43 ± 0.01

573 μm^2) were quantified for each synapse. Scale bars = 10 μm, 1 μm, and 500 nm. Data
574 are represented as the mean ± the s.e.m.
575
576 **Supplemental Table 1: Summary of condition variations tested for RAIN-STORM.**
577
578 **Supplemental Table 2: Primary antibodies used.**
579
580 **Video 1: RAIN-STORM-imaged horizontal cell shows striking neuronal arbor**
581 **detail.** Tissue was prepared for RAIN-STORM, and Calbindin-labeled horizontal cells
582 were imaged across 10μm. The image is colored depth by depth, with colors indicating
583 the axial position throughout the stack (blue 0μm to yellow 10μm). Fine neurite
584 structural detail is observed, and individual synapses are clearly visible.
585
586 **Video 2: RAIN-STORM-imaged blood vessel shows an interpericyte tunneling**
587 **nanotube bridging two vessels.** Tissue was prepared for RAIN-STORM, and collagen
588 IV-labeled vessels were imaged across 10μm. The image is colored depth by depth,
589 with colors indicating the axial position throughout the stack (blue 0μm to yellow 10μm).
590 The structure and morphology of hollow vessels are well preserved, and cross-vessel
591 nanotube connections are apparent.
592
593 **Video 3: RAIN-STORM-imaged astrocytes demonstrate fine filamentous**
594 **structures and a mesh of interacting fibers.** Tissue was prepared for RAIN-STORM,
595 and GFAP labeled astrocytes were imaged across 10μm. The image is colored depth by

596 depth, with colors indicating the axial position throughout the stack (blue 0μm to yellow
597 10μm). The structure and morphology of astrocyte filamentous fibers was observed,
598 which appear to form a highly branched network.
599
600 **Video 4: RAIN-STORM imaging of mouse bipolar neurons and ribbon synapses**
601 **reveals pre- and postsynaptic neural interactions**. Tissue was prepared for RAIN-
602 STORM, and mouse bipolar neurons in the outer plexiform layer were labeled with
603 PKCα (magenta) and pre-synaptic ribbons were labeled with RIBEYE (cyan). The image
604 is colored depth by depth, with colors indicating the axial position throughout the stack
605 (blue 0μm to yellow 10μm). Individual neurite tips can clearly be observed invaginating
606 individual presynaptic ribbons**.**
607
608 **Video 5: RAIN-STORM imaging of human bipolar neurons and ribbon synapses**
609 **shows bipolar cell interactions with ribbon synapses.** Human retina was prepared
610 for RAIN-STORM, and human bipolar neurons in the outer plexiform layer were labeled
611 with PKCα (magenta) and pre-synaptic ribbons were labeled with RIBEYE (cyan). The
612 image is colored depth by depth, with colors indicating the axial position throughout the
613 stack (blue 0μm to yellow 10μm). As in mouse sample, individual human bipolar neurite
614 tips interact with and invaginating individual presynaptic ribbons. While fewer synapses
615 were observed in the human samples relative to the mouse, it is likely that this decrease
616 is due to the inherent delay in human post-mortem sample collection rather than a
617 biologically relevant difference.
618

Figure 1 – figure supplement 1: Optical Diagram of Vutara.

Layout and optical design of the Bruker Vutara SRX352, which allows 3D STORM imaging and PSF localization via a biplane module in place of a cylindrical lens. **M**: Mirror, **DM**: Dichroic mirror, **ND**: Neutral density filter, **L**: lens, **BS**: Beam splitter, **I**: iris/aperture, **OL**: Objective lens, **EF**: Emission filter.

Figure 1 – figure supplement 2: Modifying sample conditions improves visual quality and image metrics. a-b, Representative primary data metrics (**a**) and corresponding unprocessed and processed images (**b**) are shown for variations in primary fixation concentrations. A small increase in total localizations acquired was observed with increasing concentrations of PFA, though the gain in localizations was offset by background localizations at these concentrations. Based on these parameters, 2% PFA was selected for optimized imaging. **c-d**, Representative primary data metrics (**c**) and corresponding unprocessed and processed images (**d**) are shown for variations in blocking buffer serum concentrations. In general, the best image metrics were obtained for mid-level serum concentrations (e.g. 3-5% NDS), while the lower (e.g. 1% NDS) and higher (e.g. >10%) serum concentrations resulted in either increased filtered localizations or decreased resolution overall and poorer image quality. **e-f**, Representative primary data metrics (**e**) and corresponding unprocessed and processed images (**f**) are shown for variations in imaging buffer formulations using Trolox. Increasing the Trolox concentration reduced the total amount of data collected resulting in poorer image quality relative to low Trolox concentrations (e.g. 1mM). Images are representative of those acquired from N=3 animals. Calbindin, magenta; PSD95; cyan.

642 Scale bars = 10 μm. Data are represented as the mean ± the s.e.m. Both unprocessed
643 (blue) and processed (red, OPTICS algorithm) data are shown for each dataset.
644
645 **Figure 1 – figure supplement 3: RAIN-STORM resolution as a function of sample**
646 **depth.**
647 **a**, Schematic of three image planes used to calculate sample resolution. Resolution was
648 compared in: 1) single-micron slices at the bottom of the image (nearest the objective),
649 the middle of the image stack, or at the top of the image; 2) 5μm slices from the bottom
650 of the image to the midpoint; and 3) the entirety of the 10μm stack. **b**, Sample resolution
651 quantification as a function of the three calculation methods schematized in (**a**). Planar
652 resolution (XY dimension) varies from 30.0 ± 1.6 nm to 42.5 ± 4.8 nm while resolution in
653 the axial dimensions (XZ and YZ) ranges from 46.3 ± 3.3 nm nearest the objective to
654 65.7 ± 8.5 nm farthest from the objective. N = 3. Data are represented as the mean ±
655 the s.e.m.
656
657 **Figure 2 – figure supplement 1: Confocal imaging verifies antibody specificity in**
658 **RAIN-STORM imaging.** Representative confocal images of antibodies used in this
659 study. Cellular structure and labeling patterns from confocal imaging were used as a
660 baseline with which to compare the effectiveness of RAIN-STORM imaging for various
661 targets. Scale bars = 20 μm.
662
663 **Figure 2 – figure supplement 2: RAIN-STORM imaging can be applied to diverse**
664 **array of molecular targets.** RAIN-STORM imaging of α-Tubulin, a marker for

665 cytoskeletal tubulin in the murine retina, cone arrestin, a marker for cone
666 photoreceptors, CD31, a marker for select blood vessel structures, Connexin 43, a gap
667 junction protein, Iba1, a marker for microglia, Islet1, which stains a variety of neuron cell
668 bodies, Tau, a microtubule-associated protein, Tomm20, a mitochondrial marker, and
669 VGluT1, a glutamate transporter marker for specific subsets of cells. These stains
670 demonstrate a wide variety of protein types and targets that are amenable to imaging
671 with RAIN-STORM. N = 3 animals. Scale bars = 10 and 1μm.
672
673
674 **References**

675 Alarcon-Martinez, L., Villafranca-Baughman, D., Quintero, H., Kacerovsky, J. B.,
676 Dotigny, F., Murai, K. K., Prat, A., Drapeau, P., & Di Polo, A. (2020). Interpericyte
677 tunnelling nanotubes regulate neurovascular coupling. *Nature*, *585*(7823), 91-95.
678 https://doi.org/10.1038/s41586-020-2589-x
679 Albrecht, N. E., Alevy, J., Jiang, D., Burger, C. A., Liu, B. I., Li, F., Wang, J., Kim, S. Y.,
680 Hsu, C. W., Kalaga, S., Udensi, U., Asomugha, C., Bohat, R., Gaspero, A.,
681 Justice, M. J., Westenskow, P. D., Yamamoto, S., Seavitt, J. R., Beaudet, A. L.,
682 Dickinson, M. E., & Samuel, M. A. (2018). Rapid and Integrative Discovery of
683 Retina Regulatory Molecules. *Cell Rep*, *24*(9), 2506-2519.
684 https://doi.org/10.1016/j.celrep.2018.07.090
685 Arizono, M., Inavalli, V., Panatier, A., Pfeiffer, T., Angibaud, J., Levet, F., Ter Veer, M. J.
686 T., Stobart, J., Bellocchio, L., Mikoshiba, K., Marsicano, G., Weber, B., Oliet, S.
687 H. R., & Nagerl, U. V. (2020). Structural basis of astrocytic Ca(2+) signals at

tripartite synapses. *Nat Commun*, *11*(1), 1906. https://doi.org/10.1038/s41467-020-15648-4

Bates, M., Huang, B., Dempsey, G. T., & Zhuang, X. (2007). Multicolor super-resolution imaging with photo-switchable fluorescent probes. *Science*, *317*(5845), 1749-1753. https://doi.org/10.1126/science.1146598

Bewersdorf, J., Schmidt, R., & Hell, S. W. (2006). Comparison of I5M and 4Pi-microscopy. *J Microsc*, *222*(Pt 2), 105-117. https://doi.org/10.1111/j.1365-2818.2006.01578.x

Bon, P., Linarès-Loyez, J., Feyeux, M., Alessandri, K., Lounis, B., Nassoy, P., & Cognet, L. (2018). Self-interference 3D super-resolution microscopy for deep tissue investigations. *Nat Methods*, *15*(6), 449-454. https://doi.org/10.1038/s41592-018-0005-3

Bowler, M., Kong, D., Sun, S., Nanjundappa, R., Evans, L., Farmer, V., Holland, A., Mahjoub, M. R., Sui, H., & Loncarek, J. (2019). High-resolution characterization of centriole distal appendage morphology and dynamics by correlative STORM and electron microscopy. *Nat Commun*, *10*(1), 993. https://doi.org/10.1038/s41467-018-08216-4

Celio, M. R. (1990). Calbindin D-28k and parvalbumin in the rat nervous system. *Neuroscience*, *35*(2), 375-475. https://doi.org/10.1016/0306-4522(90)90091-h

Chamma, I., Letellier, M., Butler, C., Tessier, B., Lim, K. H., Gauthereau, I., Choquet, D., Sibarita, J. B., Park, S., Sainlos, M., & Thoumine, O. (2016). Mapping the dynamics and nanoscale organization of synaptic adhesion proteins using

monomeric streptavidin. *Nat Commun*, *7*, 10773. https://doi.org/10.1038/ncomms10773

Chen, F., Tillberg, P. W., & Boyden, E. S. (2015). Optical imaging. Expansion microscopy. *Science*, *347*(6221), 543-548. https://doi.org/10.1126/science.1260088

Dembla, E., Dembla, M., Maxeiner, S., & Schmitz, F. (2020). Synaptic ribbons foster active zone stability and illumination-dependent active zone enrichment of RIM2 and Cav1.4 in photoreceptor synapses. *Sci Rep*, *10*(1), 5957. https://doi.org/10.1038/s41598-020-62734-0

Greiss, F., Deligiannaki, M., Jung, C., Gaul, U., & Braun, D. (2016). Single-Molecule Imaging in Living Drosophila Embryos with Reflected Light-Sheet Microscopy. *Biophys J*, *110*(4), 939-946. https://doi.org/10.1016/j.bpj.2015.12.035

Huang, B., Wang, W., Bates, M., & Zhuang, X. (2008). Three-dimensional super-resolution imaging by stochastic optical reconstruction microscopy. *Science*, *319*(5864), 810-813. https://doi.org/10.1126/science.1153529

Hunt, C. A., Schenker, L. J., & Kennedy, M. B. (1996). PSD-95 is associated with the postsynaptic density and not with the presynaptic membrane at forebrain synapses. *J Neurosci*, *16*(4), 1380-1388. https://www.ncbi.nlm.nih.gov/pubmed/8778289

Juette, M. F., Gould, T. J., Lessard, M. D., Mlodzianoski, M. J., Nagpure, B. S., Bennett, B. T., Hess, S. T., & Bewersdorf, J. (2008). Three-dimensional sub-100 nm resolution fluorescence microscopy of thick samples. *Nat Methods*, *5*(6), 527-529. https://doi.org/10.1038/nmeth.1211

733 Koulen, P., Fletcher, E. L., Craven, S. E., Bredt, D. S., & Wässle, H. (1998).
734 Immunocytochemical localization of the postsynaptic density protein PSD-95 in
735 the mammalian retina. *J Neurosci*, *18*(23), 10136-10149.
736 https://www.ncbi.nlm.nih.gov/pubmed/9822767
737 Ku, T., Swaney, J., Park, J. Y., Albanese, A., Murray, E., Cho, J. H., Park, Y. G.,
738 Mangena, V., Chen, J., & Chung, K. (2016). Multiplexed and scalable super-
739 resolution imaging of three-dimensional protein localization in size-adjustable
740 tissues. *Nat Biotechnol*, *34*(9), 973-981. https://doi.org/10.1038/nbt.3641
741 Leterrier, C., Potier, J., Caillol, G., Debarnot, C., Rueda Boroni, F., & Dargent, B.
742 (2015). Nanoscale Architecture of the Axon Initial Segment Reveals an
743 Organized and Robust Scaffold. *Cell Rep*, *13*(12), 2781-2793.
744 https://doi.org/10.1016/j.celrep.2015.11.051
745 Li, S., Mitchell, J., Briggs, D. J., Young, J. K., Long, S. S., & Fuerst, P. G. (2016).
746 Morphological Diversity of the Rod Spherule: A Study of Serially Reconstructed
747 Electron Micrographs. *PLoS One*, *11*(3), e0150024.
748 https://doi.org/10.1371/journal.pone.0150024
749 Micheva, K. D., & Smith, S. J. (2007). Array tomography: a new tool for imaging the
750 molecular architecture and ultrastructure of neural circuits. *Neuron*, *55*(1), 25-36.
751 https://doi.org/10.1016/j.neuron.2007.06.014
752 Mikhaylova, M., Cloin, B. M., Finan, K., van den Berg, R., Teeuw, J., Kijanka, M. M.,
753 Sokolowski, M., Katrukha, E. A., Maidorn, M., Opazo, F., Moutel, S., Vantard, M.,
754 Perez, F., van Bergen en Henegouwen, P. M., Hoogenraad, C. C., Ewers, H., &

Kapitein, L. C. (2015). Resolving bundled microtubules using anti-tubulin nanobodies. *Nat Commun*, *6*, 7933. https://doi.org/10.1038/ncomms8933

Mlodzianoski, M. J., Cheng-Hathaway, P. J., Bemiller, S. M., McCray, T. J., Liu, S., Miller, D. A., Lamb, B. T., Landreth, G. E., & Huang, F. (2018). Active PSF shaping and adaptive optics enable volumetric localization microscopy through brain sections. *Nat Methods*, *15*(8), 583-586. https://doi.org/10.1038/s41592-018-0053-8

Mönkemöller, V., Øie, C., Hübner, W., Huser, T., & McCourt, P. (2015). Multimodal super-resolution optical microscopy visualizes the close connection between membrane and the cytoskeleton in liver sinusoidal endothelial cell fenestrations. *Sci Rep*, *5*, 16279. https://doi.org/10.1038/srep16279

Moser, T., Grabner, C. P., & Schmitz, F. (2020). Sensory Processing at Ribbon Synapses in the Retina and the Cochlea. *Physiol Rev*, *100*(1), 103-144. https://doi.org/10.1152/physrev.00026.2018

Nanguneri, S., Flottmann, B., Horstmann, H., Heilemann, M., & Kuner, T. (2012). Three-dimensional, tomographic super-resolution fluorescence imaging of serially sectioned thick samples. *PLoS One*, *7*(5), e38098. https://doi.org/10.1371/journal.pone.0038098

Nehme, E., Freedman, D., Gordon, R., Ferdman, B., Weiss, L. E., Alalouf, O., Naor, T., Orange, R., Michaeli, T., & Shechtman, Y. (2020). DeepSTORM3D: dense 3D localization microscopy and PSF design by deep learning. *Nat Methods*, *17*(7), 734-740. https://doi.org/10.1038/s41592-020-0853-5

777 Nieuwenhuizen, R. P., Lidke, K. A., Bates, M., Puig, D. L., Grunwald, D., Stallinga, S., &
778 Rieger, B. (2013). Measuring image resolution in optical nanoscopy. *Nat*
779 *Methods*, *10*(6), 557-562. https://doi.org/10.1038/nmeth.2448
780 O'Sullivan, M. L., Punal, V. M., Kerstein, P. C., Brzezinski, J. A. t., Glaser, T., Wright, K.
781 M., & Kay, J. N. (2017). Astrocytes follow ganglion cell axons to establish an
782 angiogenic template during retinal development. *Glia*, *65*(10), 1697-1716.
783 https://doi.org/10.1002/glia.23189
784 Pavani, S. R., Thompson, M. A., Biteen, J. S., Lord, S. J., Liu, N., Twieg, R. J., Piestun,
785 R., & Moerner, W. E. (2009). Three-dimensional, single-molecule fluorescence
786 imaging beyond the diffraction limit by using a double-helix point spread function.
787 *Proc Natl Acad Sci U S A*, *106*(9), 2995-2999.
788 https://doi.org/10.1073/pnas.0900245106
789 Punge, A., Rizzoli, S. O., Jahn, R., Wildanger, J. D., Meyer, L., Schönle, A., Kastrup, L.,
790 & Hell, S. W. (2008). 3D reconstruction of high-resolution STED microscope
791 images. *Microsc Res Tech*, *71*(9), 644-650. https://doi.org/10.1002/jemt.20602
792 Sanes, J. R., & Zipursky, S. L. (2010). Design principles of insect and vertebrate visual
793 systems. *Neuron*, *66*(1), 15-36. https://doi.org/10.1016/j.neuron.2010.01.018
794 Schmitz, F., & Drenckhahn, D. (1997). Dystrophin in the retina. *Prog Neurobiol*, *53*(5),
795 547-560. https://doi.org/10.1016/s0301-0082(97)00047-6
796 Sigal, Y. M., Speer, C. M., Babcock, H. P., & Zhuang, X. (2015). Mapping Synaptic
797 Input Fields of Neurons with Super-Resolution Imaging. *Cell*, *163*(2), 493-505.
798 https://doi.org/10.1016/j.cell.2015.08.033

799 Stahley, S. N., Bartle, E. I., Atkinson, C. E., Kowalczyk, A. P., & Mattheyses, A. L.
800 (2016). Molecular organization of the desmosome as revealed by direct
801 stochastic optical reconstruction microscopy. *J Cell Sci*, *129*(15), 2897-2904.
802 https://doi.org/10.1242/jcs.185785
803 Suleiman, H., Zhang, L., Roth, R., Heuser, J. E., Miner, J. H., Shaw, A. S., & Dani, A.
804 (2013). Nanoscale protein architecture of the kidney glomerular basement
805 membrane. *Elife*, *2*, e01149. https://doi.org/10.7554/eLife.01149
806 Tao, C., & Zhang, X. (2016). Retinal Proteoglycans Act as Cellular Receptors for
807 Basement Membrane Assembly to Control Astrocyte Migration and
808 Angiogenesis. *Cell Rep*, *17*(7), 1832-1844.
809 https://doi.org/10.1016/j.celrep.2016.10.035
810 Tillberg, P. W., Chen, F., Piatkevich, K. D., Zhao, Y., Yu, C. C., English, B. P., Gao, L.,
811 Martorell, A., Suk, H. J., Yoshida, F., DeGennaro, E. M., Roossien, D. H., Gong,
812 G., Seneviratne, U., Tannenbaum, S. R., Desimone, R., Cai, D., & Boyden, E. S.
813 (2016). Protein-retention expansion microscopy of cells and tissues labeled using
814 standard fluorescent proteins and antibodies. *Nat Biotechnol*, *34*(9), 987-992.
815 https://doi.org/10.1038/nbt.3625
816 Uesugi, R., Yamada, M., Mizuguchi, M., Baimbridge, K. G., & Kim, S. U. (1992).
817 Calbindin D-28k and parvalbumin immunohistochemistry in developing rat retina.
818 *Exp Eye Res*, *54*(4), 491-499. https://doi.org/10.1016/0014-4835(92)90127-e
819 van den Dries, K., Schwartz, S. L., Byars, J., Meddens, M. B., Bolomini-Vittori, M.,
820 Lidke, D. S., Figdor, C. G., Lidke, K. A., & Cambi, A. (2013). Dual-color
821 superresolution microscopy reveals nanoscale organization of mechanosensory

podosomes. *Mol Biol Cell*, *24*(13), 2112-2123. https://doi.org/10.1091/mbc.E12-12-0856

Xu, J., Tehrani, K. F., & Kner, P. (2015). Multicolor 3D super-resolution imaging by quantum dot stochastic optical reconstruction microscopy. *ACS Nano*, *9*(3), 2917-2925. https://doi.org/10.1021/nn506952g

Figure 1: 3D Imaging of neurons in tissue.

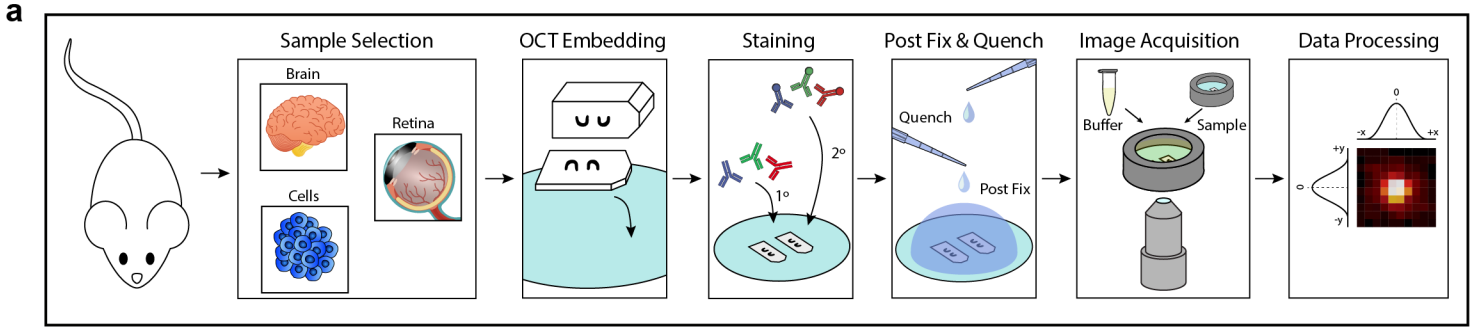

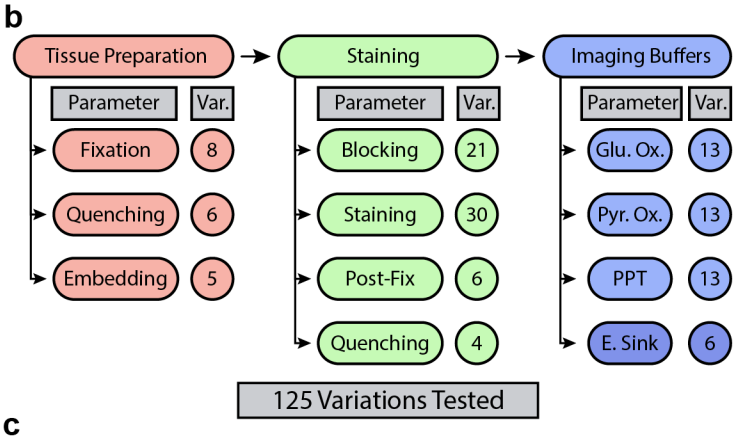

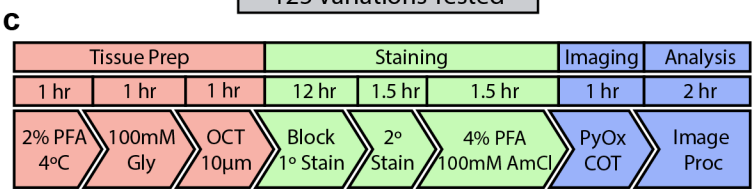

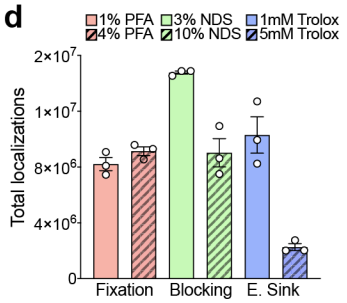

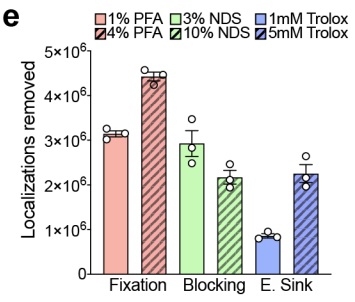

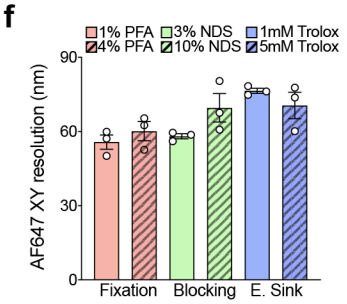

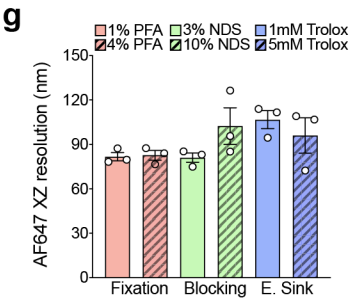

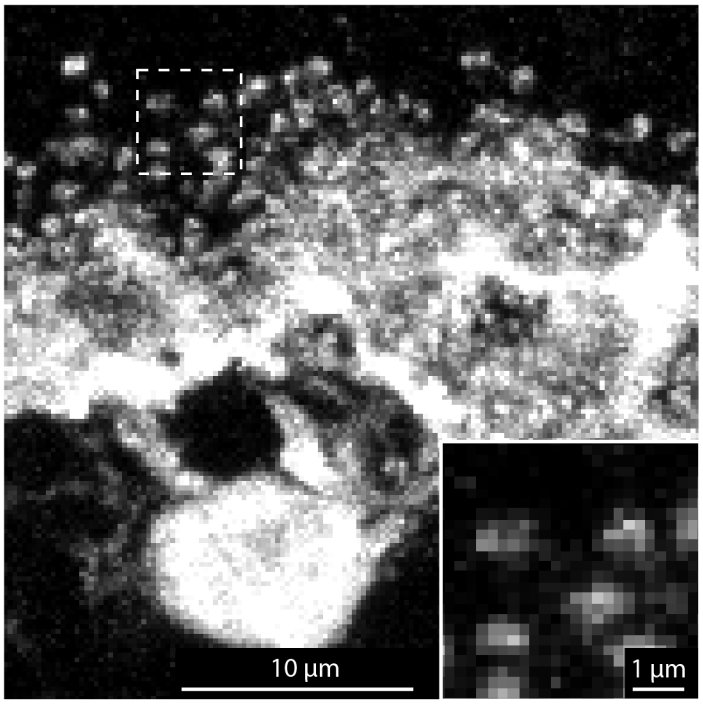

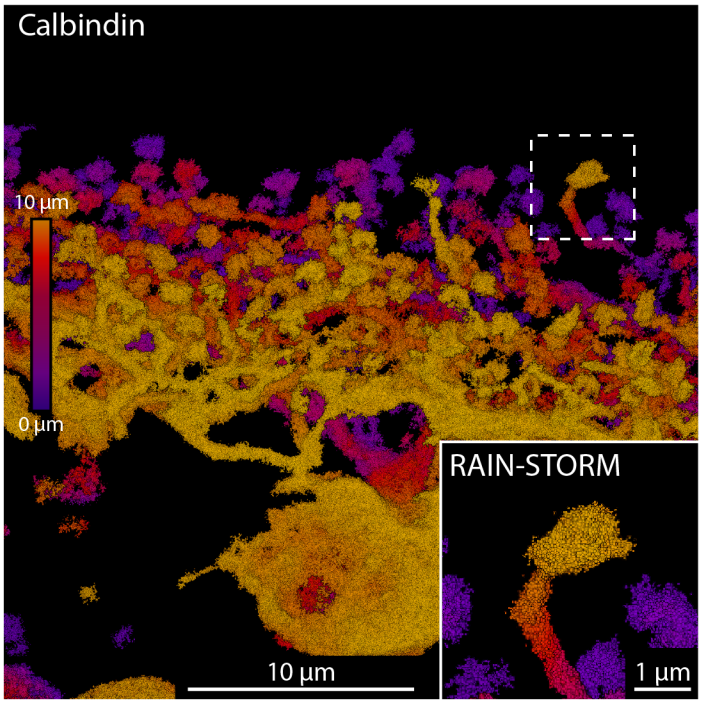

Figure 2: RAIN-STORM delivers robust imaging for a diverse array of molecular targets in tissue.

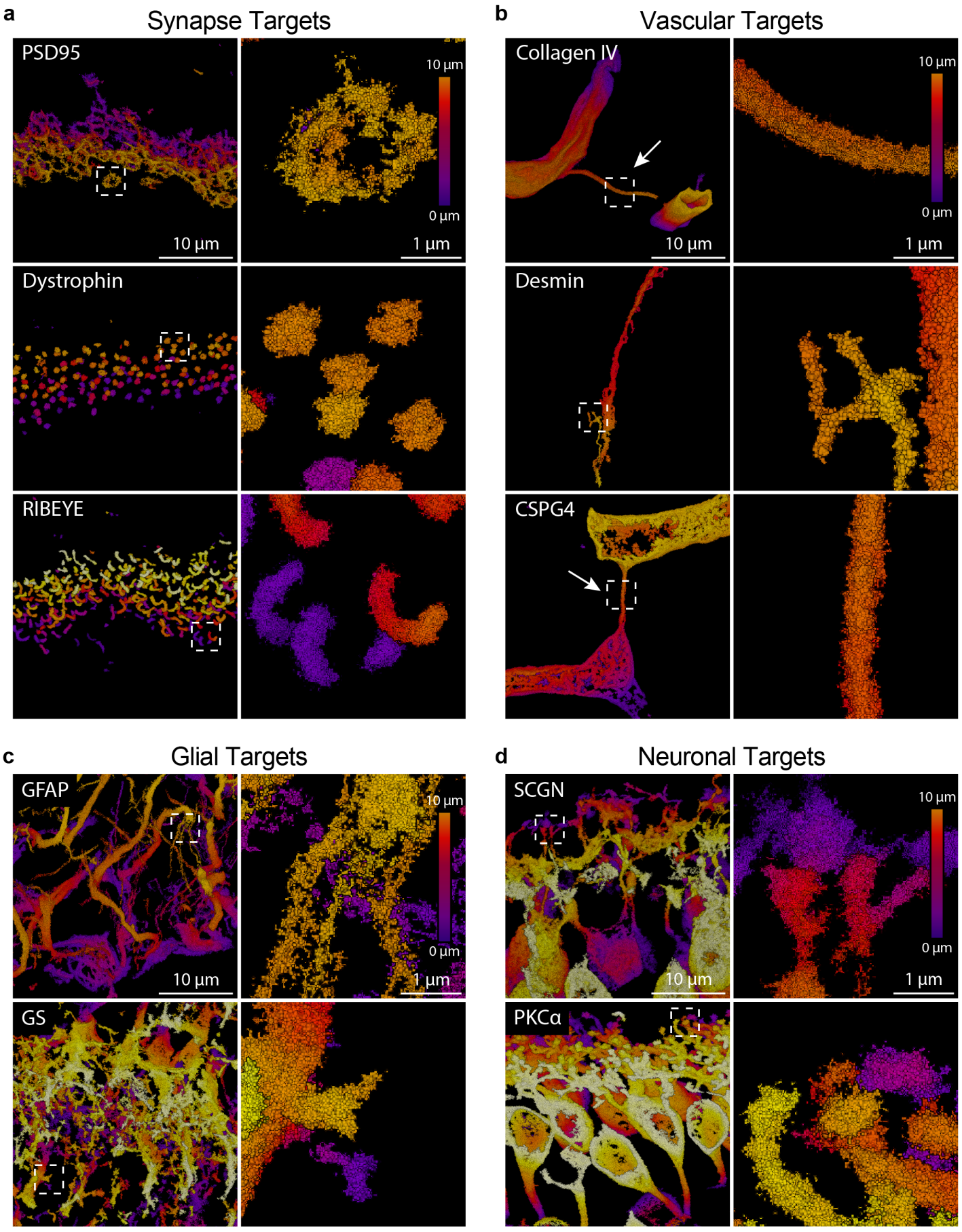

Figure 3: RAIN-STORM enables dual-channel super resolution imaging among diverse species.

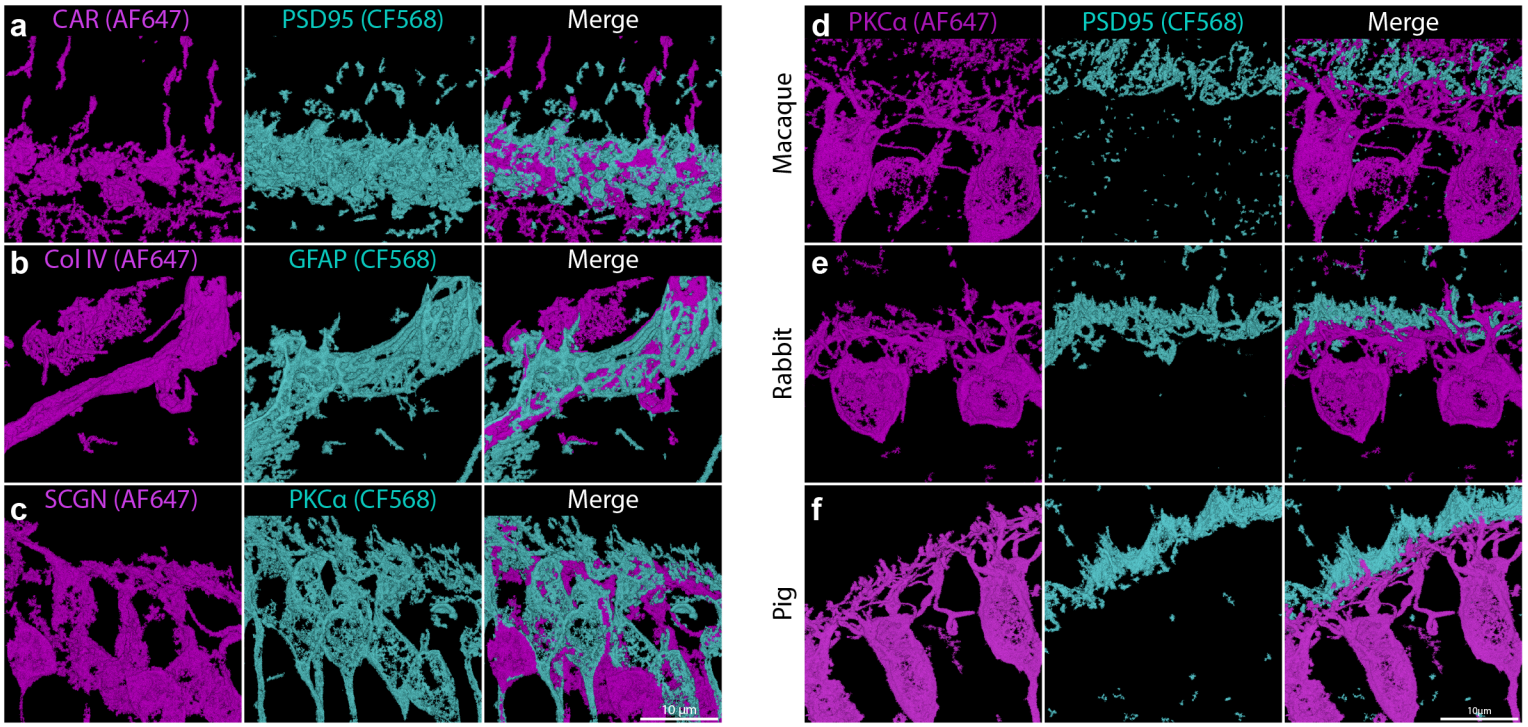

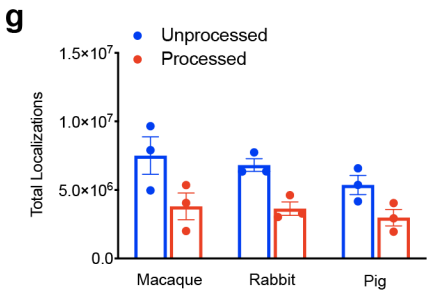

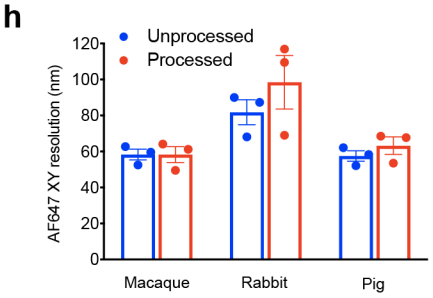

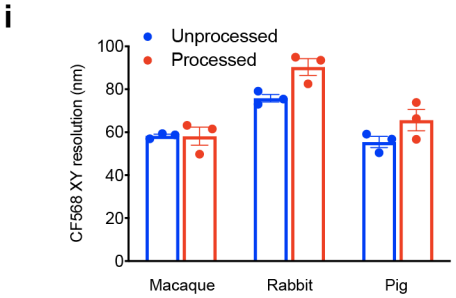

Figure 4: RAIN-STORM resolves structural and molecular features of synapses.

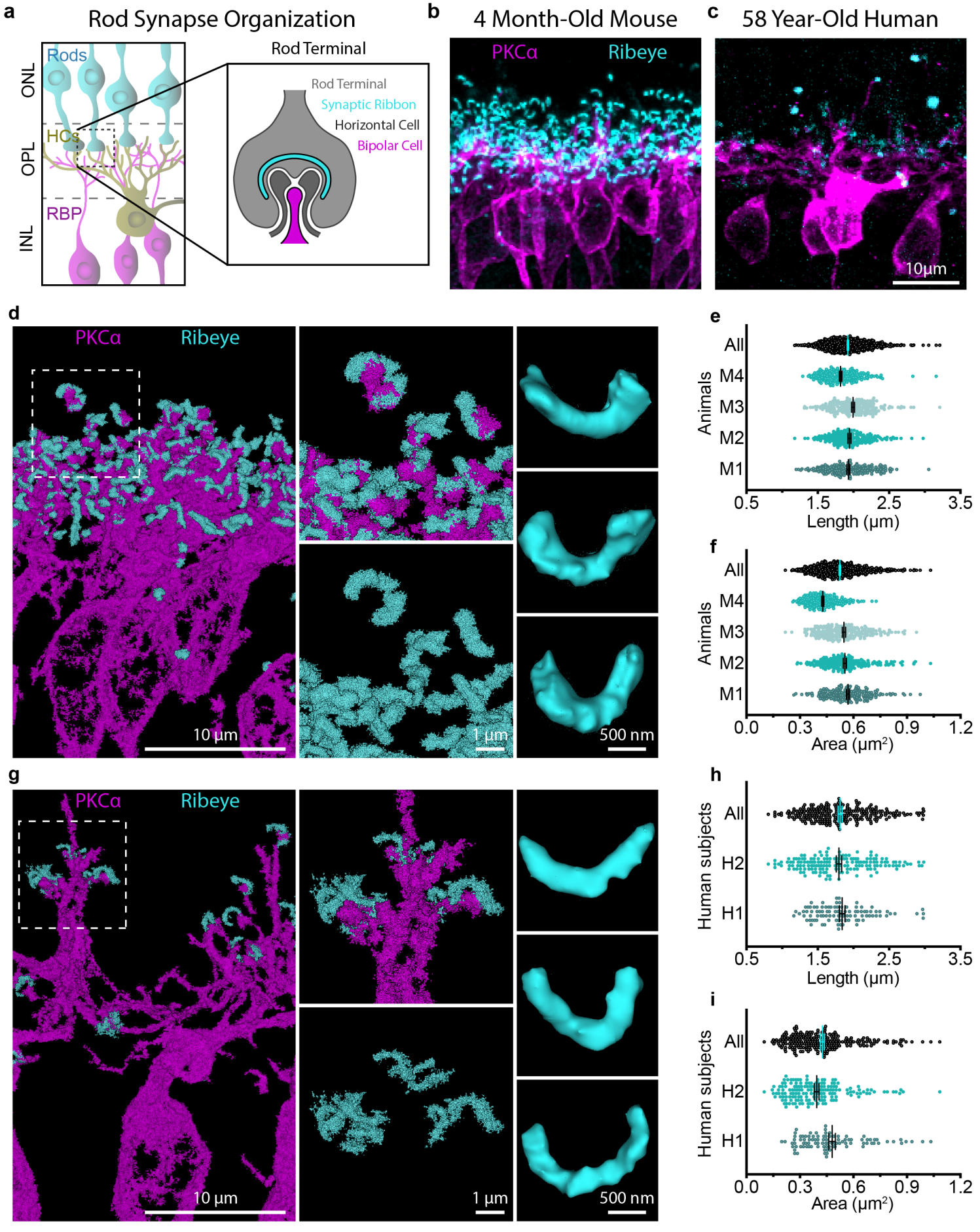

Figure 1 - Figure Supplement 1. Optical Diagram of Vutara.

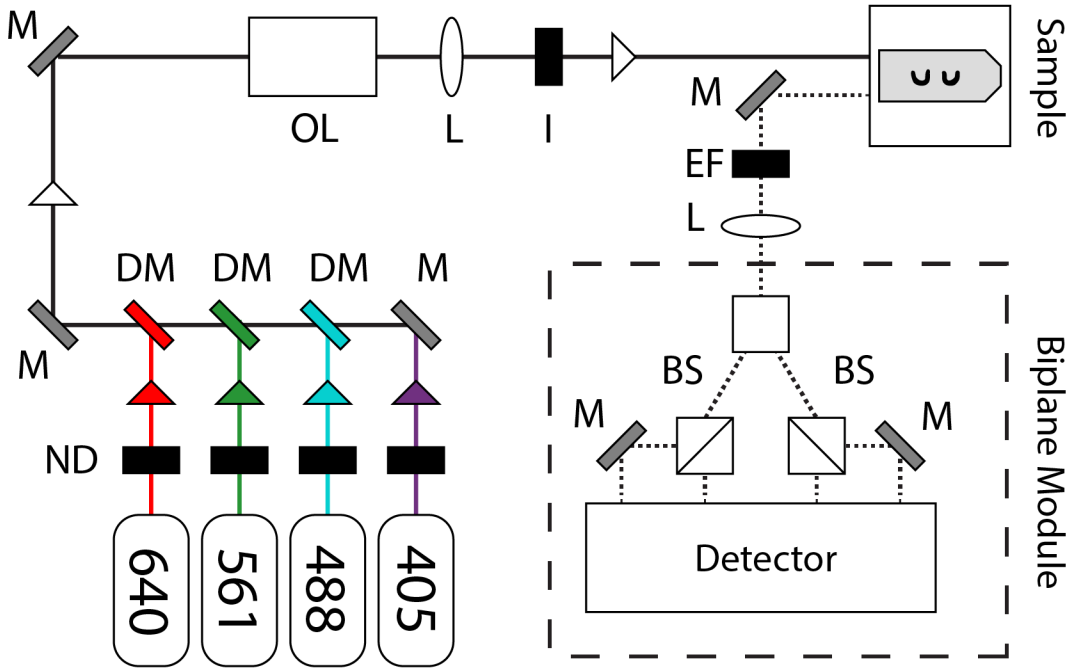

Figure 1 - Figure Supplement 2. Modifying sample conditions improves visual quality and image metrics.

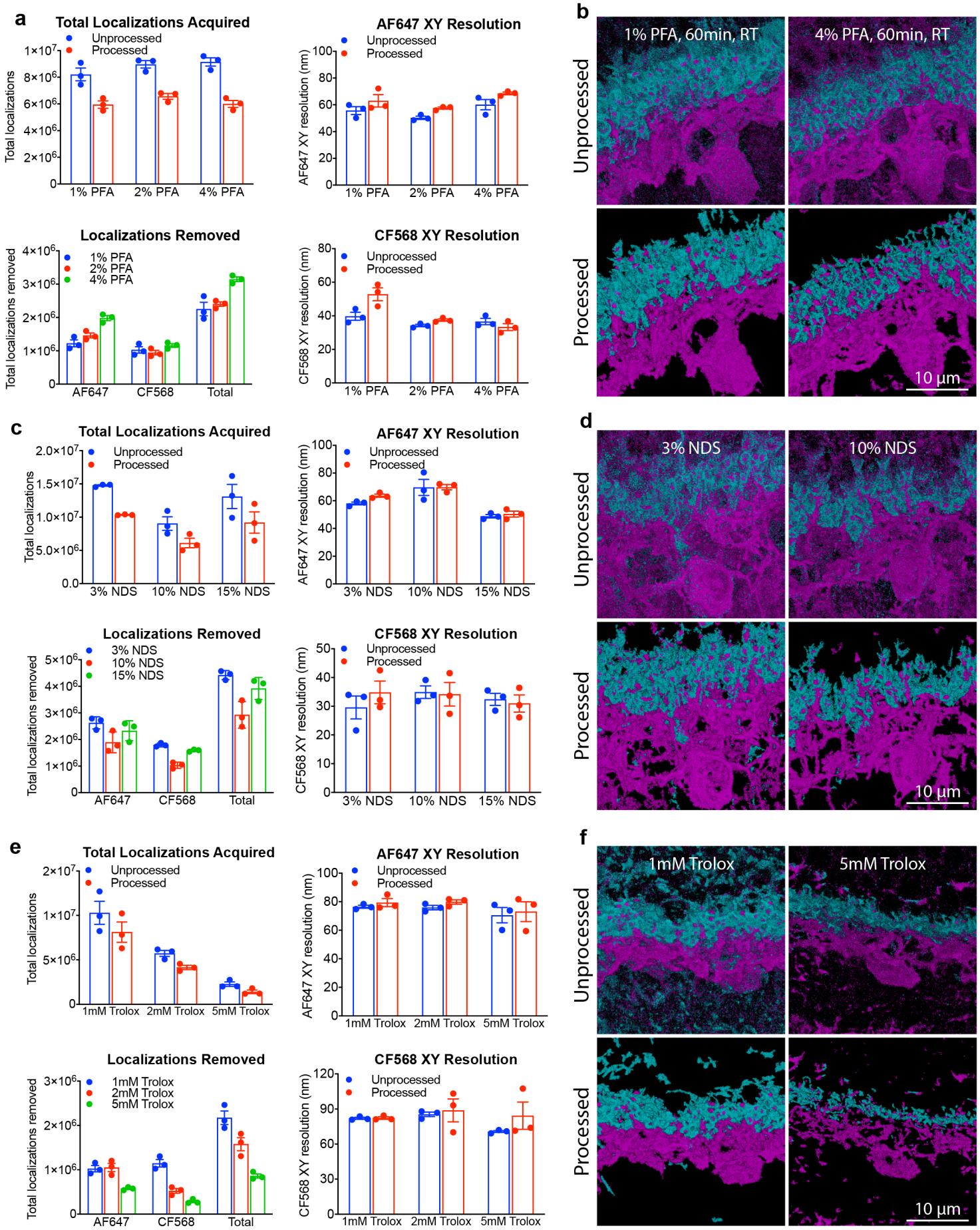

Figure 1 - Figure Supplement 3: RAIN-STORM resolution as a function of sample depth.

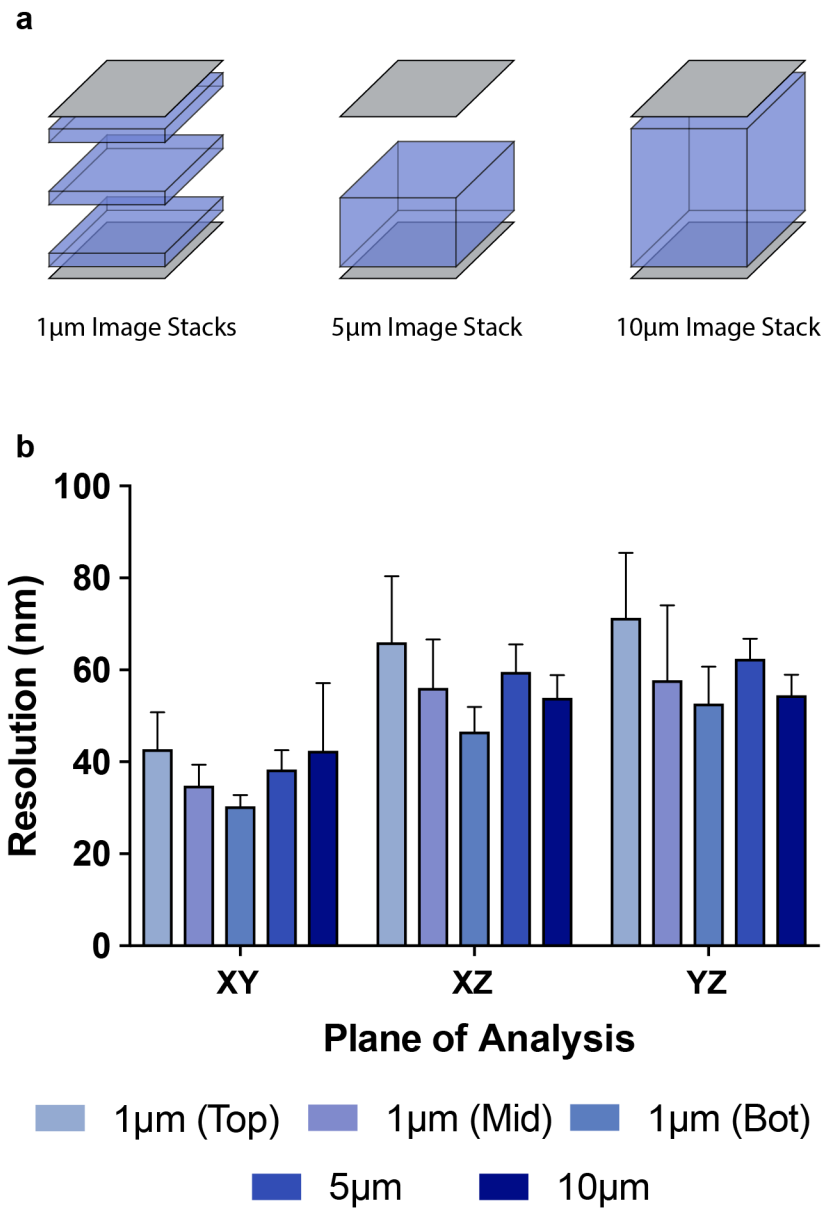

Figure 2 - Figure Supplement 1. Confocal imaging verifies antibody specificity in RAIN-STORM imaging.

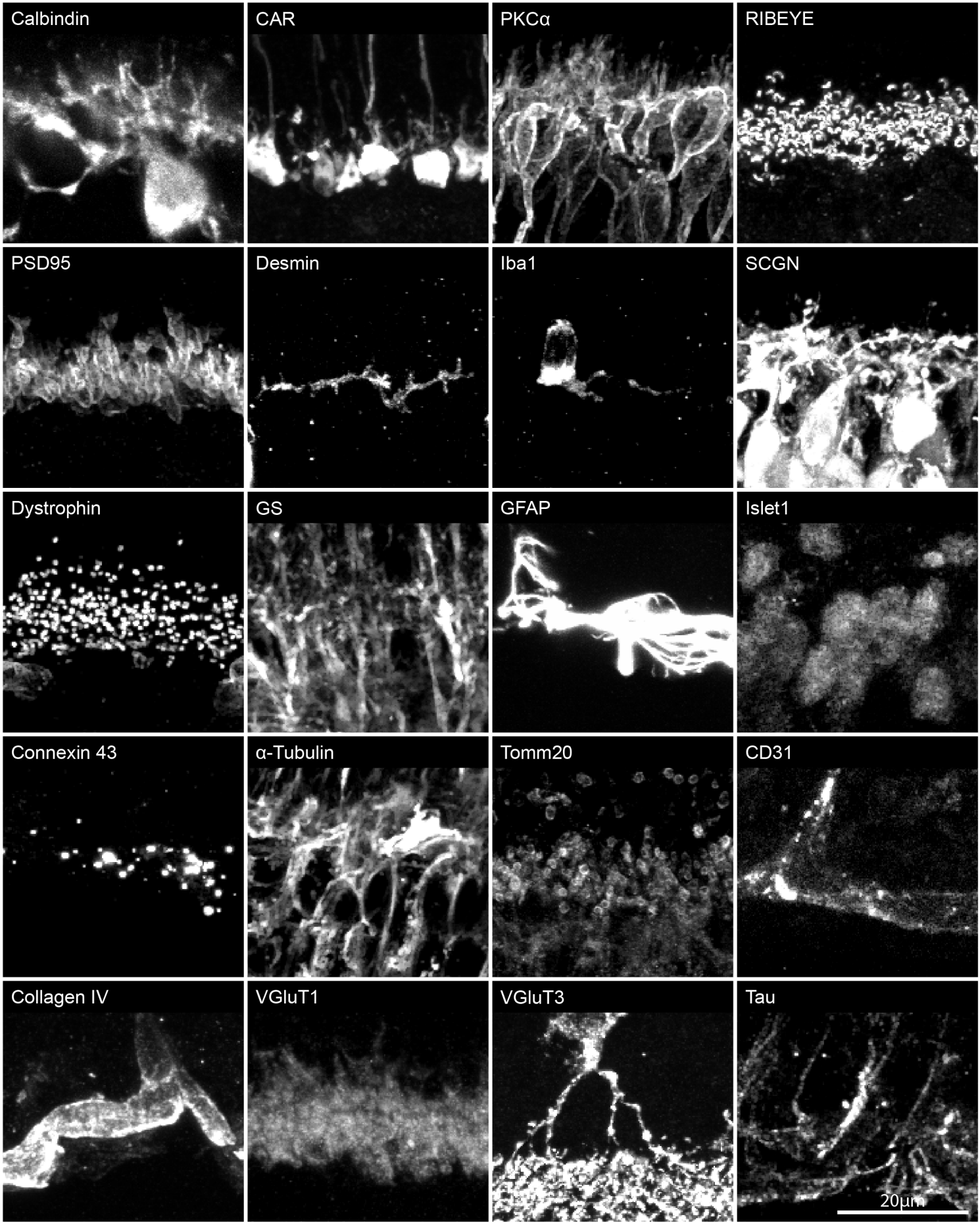

Figure 2 - Figure Supplement 2. RAIN-STORM imaging can be applied to a diverse array of molecular targets.

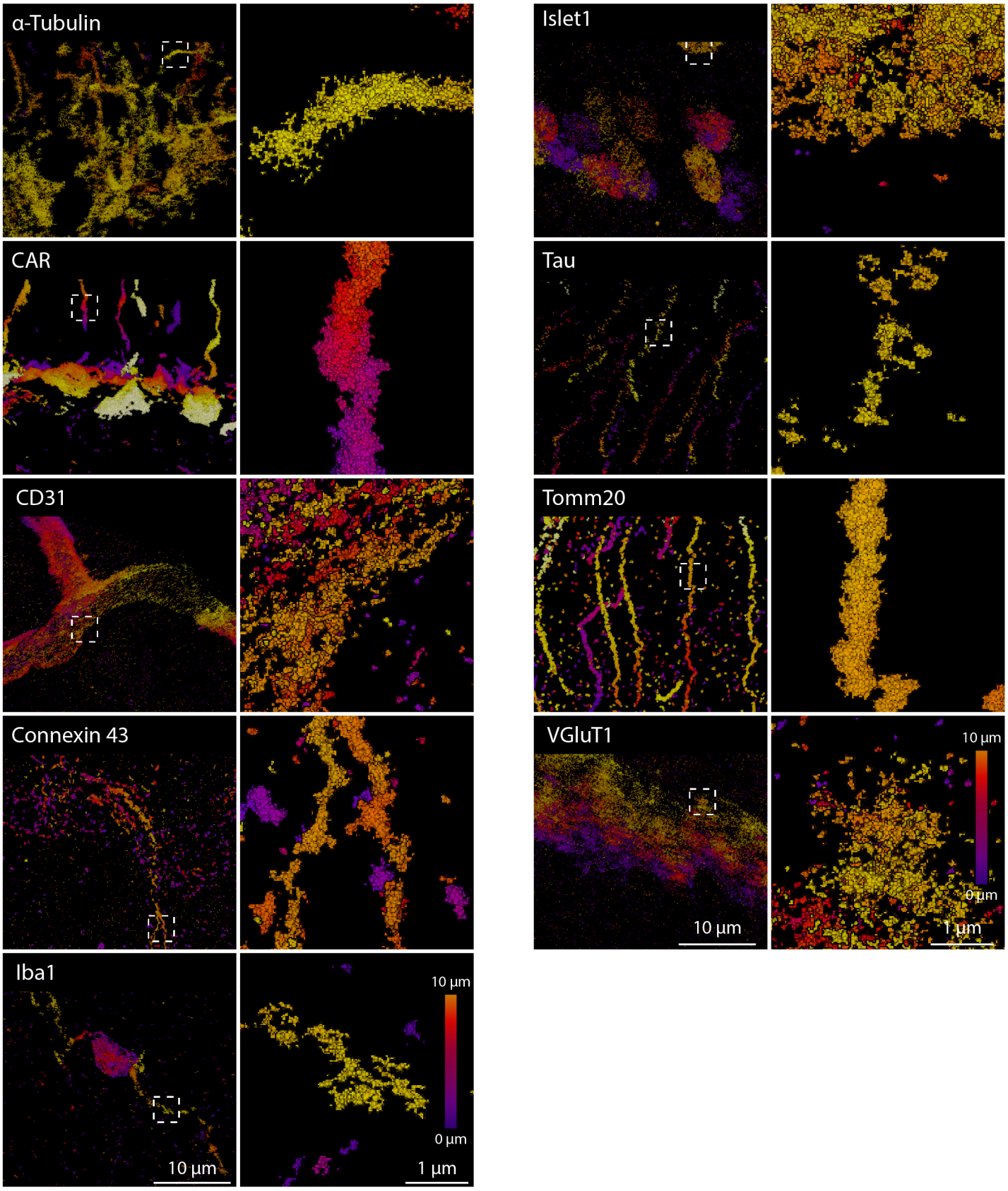

Supplemental Table 1: Summary of condition variations tested for RAIN-STORM.

Stage	Parameter	Variations	Specifics	Total Localizations Acquired	Background Localizations	AF647 XY Res	CF568 XY Res
Tissue Preparation	Primary Fixation	Conc./Temp	1% PFA, RT, 60min	8213357	2998284	56.7234	39.7970
			2% PFA, RT, 60 min	8970285	2398174	50.3231	34.2027
			4% PFA, RT, 60 min	9146043	3144002	60.1768	36.6071
			4% PFA, 4C, 60 min	6779812	2792175	56.5597	35.5531
		Type	0% PFA, 0.3% GA, RT, 60 min	4914685	3059107	38.5014	27.1380
			2% PFA, 0.3% GA, RT, 60 min	5030786	3181862	45.1080	29.3187
		Timing	4% PFA, RT, 30 min	8642310	3722096	54.3354	31.3137
			4% PFA, RT, 120 min	10108757	3498380	48.5256	32.5775
	Primary Quenching	Conc./Type	10mM Glycine	9751623	2847049	51.7930	31.7254
			100mM Glycine	12209377	3525533	63.2148	37.2768
		Conc./Type	10mM NH3Cl	9751623	3043674	50.2599	39.2483
			100mM NH3Cl	11649151	3425099	55.7147	37.4105
		Conc./Type	0.1% NaBH4	10066425	2222657	53.5908	37.7183
			0.5% NaBH4	11156141	2673369	52.2041	32.6448
	Embedding Method	Thickness	10µm	9146043	3144002	60.1768	36.6071
			20µm	3775049	2494498	63.0147	66.6873
	Blocking Buffer	Serum	1% NDS	12554580	3953868	59.1086	29.2762
			3% NDS	14772343	4423472	58.0771	29.6001
			5% NDS	10276383	3368744	53.7408	30.4973
			10% NDS	9029693	2928266	69.5874	34.9191
			15% NDS	13109963	3920780	48.8157	32.4246
		Permeabilizer Type	0.1% Triton	9958189	3309736	57.0414	25.8641
			0.3% Triton	13145415	4107653	60.7596	35.5746
			0.5% Triton	9647404	3040177	57.8182	35.4601
			1.0% Triton	10495550	3487400	50.3823	30.9056
			2.0% Triton	10179749	3443009	50.8491	27.7015
		Permeabilizer Type	0.1% Saponin	7443945	3638582	43.9059	26.9830
			0.3% Saponin	6084083	2769395	48.9074	33.9253
			0.5% Saponin	6343524	2916079	64.1917	41.0107
			1.0% Saponin	7614606	3039943	50.7969	32.2521
			2.0% Saponin	6171508	2849269	71.0758	38.7984
	Blocking Step	Time	No Block	6165974	2671417	41.6942	37.3806
		Temp/Time	4°C, 30 min	5067694	2089784	45.6442	35.7788
			4°C, 120 min	5032729	2042575	45.9341	35.4185
		Temp/Time	RT, 30 min	5802683	2586804	43.9987	42.6722
			RT, 120 min	5932099	2392430	48.0725	34.6311
Staining	Primary Antibody	Protein Targets	Calbindin				
			CAR				
			PKCa				
			Ribeye				
			PSD95				
			Desmin				
			Iba1				
			SCGN				
			Dystrophin				
			GS				
			GFAP	N/A	N/A	N/A	N/A
			Iste1				
			Connexin43				
			a-Tubulin				
			Tomm20				
			CD31				
			Collagen IV				
			VGluT1				
			VGlut3				
			Tau				
			NG2				
	Secondary Antibody	Fluorophore/Conc.	AF647 1:100	6073156	1867141	65.7862	
			AF647 1:1000	3739319	1475533	43.9605	N/A
			AF647 1:5000	1185205	478033	38.4452	
		Fluorophore/Conc.	CF568 1:100	6326942	2239627		30.8011
			CF568 1:1000	3430488	1453105	N/A	35.4525
			CF568 1:5000	855764	445964		29.7523
	Post-Fixation	Conc./Time	1% PFA, 10 min	6260957	2373438	46.1414	35.8572
			2% PFA, 10 min	6750477	2604387	48.1055	32.2951
			4% PFA, 10 min	8659132	3367457	54.9271	36.2804
		Conc./Time	1% PFA, 30 min	5374777	2091335	55.6734	33.1415
			2% PFA, 30 min	7270614	2700060	54.2458	42.6215
			4% PFA, 30 min	8267553	2996594	47.6018	35.7969
	Post-Quenching	Conc./Type	10mM Glycine	5330971	1691966	65.6889	55.4278
			100mM Glycine	5636215	1918352	46.5097	44.4271
		Conc./Type	10mM NH3Cl	4791254	2077605	55.6635	46.1726
			100mM NH3Cl	5010685	1932905	50.5240	43.5233
Imaging	GLOX	BME	0mM BME	13030311	3553994	78.36503	61.88587
			71.5mM BME	10612112	2539832	70.96077	46.30657
			143mM BME	11193541	2723165	86.47950	68.97667
			286mM BME	9332914	2006797	73.10220	72.54603
		Catalase	0U Catalase	7104374	1453545	77.87803	71.28623
			20U Catalase	7137281	2047426	72.29080	76.41330
			100U Catalase	9595769	2075109	84.14287	65.44140
		Glucose Ox.	500U Catalase	10195843	2537068	71.02247	64.64657
			0U Glu. Ox.	7104374	1453545	77.87803	71.28623
			10U Glu. Ox.	7137281	2047426	72.29080	76.41330
			200U Glu. Ox.	9595769	2075109	84.14287	65.44140
			40U Glu. Ox.	10195843	2537068	71.02247	64.64657
	PPT	MEA	0mM MEA	10036933	2362114	82.48007	67.48763
			10mM MEA	11484612	2540791	74.56670	73.96387
			20mM MEA	8917782	2567084	71.94410	66.66003
			40mM MEA	9962371	2736129	73.49853	75.80517
		BME	0mM BME	6344927	2172067	63.94573	44.79663
			71.5mM BME	6632177	2110500	75.79637	55.62603
			143mM BME	6865185	1935796	71.76753	63.42270
			286mM BME	6990130	2025152	64.24200	49.40647
		PCD	0U PCD	1879393	1100339	50.68107	42.61873
			~0.09U PCD	3218723	1402939	68.00433	55.09720
			~0.17U PCD	3176465	1258718	71.34050	60.59277
			~0.35U PCD	2138172	1068920	53.55533	44.69093
		MEA	0mM MEA	4388805	1545313	53.90987	54.86183
			10mM MEA	4151177	1465681	73.73497	60.26230
			20mM MEA	3063824	1336807	70.74163	56.03840
			40mM MEA	2834421	1417678	58.42780	54.52740
		PCA	0mM PCA	1501576	997725	62.61477	45.58707
			1mM PCA	4425433	1679832	74.27553	74.12297
			2mM PCA	3473790	1608543	72.50673	65.05123
			4mM PCA	2099282	1104718	72.42587	63.55333
	POC	BME	0mM BME	6344927	2172067	63.9457	44.7966
			71.5mM BME	6632177	2110500	75.7964	55.6260
			143mM BME	6865185	1935796	71.7675	63.4227
			286mM BME	6990130	2025152	64.2420	49.4065
		Pyranose Ox.	0U Py. Ox.	5160037	1609622	69.9593	44.6356
			1U Py. Ox.	7348113	1753947	85.9037	59.7095
			5U Py. Ox.	6057925	1699933	80.5024	60.1876
			10U Py. Ox.	7268535	2161980	82.4528	59.1651
		MEA	0mM MEA	8838811	2172407	85.3317	60.0705
			10mM MEA	6045768	1873840	77.7011	52.7179
			20mM MEA	6072468	2293750	73.6791	55.3963
			40mM MEA	6479168	1771027	74.9191	50.7731
		Catalase	0U Catalase	6053582	1916468	67.6008	57.5033
			20U Catalase	8486951	2078212	88.8667	63.1553
			100U Catalase	7462499	2063145	83.4481	58.2703
			500U Catalase	8097364	2179157	79.8765	50.1370
		Electron Sinks	1mM Trolox	10297129	2172781	76.4754	82.0630
		Conc./Type	2mM Trolox	5733708	1578968	75.8681	85.4778
			5mM Trolox	2270131	862325	70.5364	70.7546
		Conc./Type	1mM COT	7249814	2213086	68.4071	58.4930
			2mM COT	8668903	1677820	79.6488	78.9307
			5mM COT	7412183	1543031	76.8966	62.1923
Optimized RAIN-STORM				12804183.3333	7082472.0000	61.1141	31.2234

Condition specification

1% PFA RT 60 min, No Quench, 10µm section, 3% NDS, 0.3% Triton, 60min RT Block, 1:1000 Pri Dil 12 hr, 1:1000 Sec Dil 60min, No Postfix, No Postfix Quench, 20U Glu. Ox. 71.5mM BME, 100U Catalase, 20mM MEA, 200nm Step size,250f, 3 cycle, 0.16µm, 25p
2% PFA RT 60 min, No Quench, 10µm section, 3% NDS, 0.3% Triton, 60min RT Block, 1:1000 Pri Dil 12 hr, 1:1000 Sec Dil 60min, No Postfix, No Postfix Quench, 20U Glu. Ox. 71.5mM BME, 100U Catalase, 20mM MEA, 200nm Step size,250f, 3 cycle, 0.16µm, 25p
4% PFA RT 60 min, No Quench, 10µm section, 3% NDS, 0.3% Triton, 60min RT Block, 1:1000 Pri Dil 12 hr, 1:1000 Sec Dil 60min, No Postfix, No Postfix Quench, 20U Glu. Ox. 71.5mM BME, 100U Catalase, 20mM MEA, 200nm Step size,250f, 3 cycle, 0.16µm, 25p
4% PFA 4C 60 min, No Quench, 10µm section, 3% NDS, 0.3% Triton, 60min RT Block, 1:1000 Pri Dil 12 hr, 1:1000 Sec Dil 60min, No Postfix, No Postfix Quench, 20U Glu. Ox. 71.5mM BME, 100U Catalase, 20mM MEA, 200nm Step size,250f, 3 cycle, 0.16µm, 25p
0% PFA 0.3% GA RT 60 min, No Quench, 10µm section, 3% NDS, 0.3% Triton, 60min RT Block, 1:1000 Pri Dil 12 hr, 1:1000 Sec Dil 60min, No Postfix, No Postfix Quench, 20U Glu. Ox. 71.5mM BME, 100U Catalase, 20mM MEA, 200nm Step size,250f, 3 cycle, 0.16µm, 25p
2% PFA 0.3% GA RT 60 min, No Quench, 10µm section, 3% NDS, 0.3% Triton, 60min RT Block, 1:1000 Pri Dil 12 hr, 1:1000 Sec Dil 60min, No Postfix, No Postfix Quench, 20U Glu. Ox. 71.5mM BME, 100U Catalase, 20mM MEA, 200nm Step size,250f, 3 cycle, 0.16µm, 25p
4% PFA RT 30 min, No Quench, 10µm section, 3% NDS, 0.3% Triton, 60min RT Block, 1:1000 Pri Dil 12 hr, 1:1000 Sec Dil 60min, No Postfix, No Postfix Quench, 20U Glu. Ox. 71.5mM BME, 100U Catalase, 20mM MEA, 200nm Step size,250f, 3 cycle, 0.16µm, 25p
4% PFA RT 120 min, No Quench, 10µm section, 3% NDS, 0.3% Triton, 60min RT Block, 1:1000 Pri Dil 12 hr, 1:1000 Sec Dil 60min, No Postfix, No Postfix Quench, 20U Glu. Ox. 71.5mM BME, 100U Catalase, 20mM MEA, 200nm Step size,250f, 3 cycle, 0.16µm, 25p
4% PFA RT 60 min, 10mM Glycine, 10µm section, 3% NDS, 0.3% Triton, 60min RT Block, 1:1000 Pri Dil 12 hr, 1:1000 Sec Dil 60min, No Postfix, No Postfix Quench, 20U Glu. Ox. 71.5mM BME, 100U Catalase, 20mM MEA, 200nm Step size,250f, 3 cycle, 0.16µm, 25p
4% PFA RT 60 min, 100mM Glycine, 10µm section, 3% NDS, 0.3% Triton, 60min RT Block, 1:1000 Pri Dil 12 hr, 1:1000 Sec Dil 60min, No Postfix, No Postfix Quench, 20U Glu. Ox. 71.5mM BME, 100U Catalase, 20mM MEA, 200nm Step size,250f, 3 cycle, 0.16µm, 25p
4% PFA RT 60 min, 10mM NH3Cl, 10µm section, 3% NDS, 0.3% Triton, 60min RT Block, 1:1000 Pri Dil 12 hr, 1:1000 Sec Dil 60min, No Postfix, No Postfix Quench, 20U Glu. Ox. 71.5mM BME, 100U Catalase, 20mM MEA, 200nm Step size,250f, 3 cycle, 0.16µm, 25p
4% PFA RT 60 min, 100mM NH3Cl, 10µm section, 3% NDS, 0.3% Triton, 60min RT Block, 1:1000 Pri Dil 12 hr, 1:1000 Sec Dil 60min, No Postfix, No Postfix Quench, 20U Glu. Ox. 71.5mM BME, 100U Catalase, 20mM MEA, 200nm Step size,250f, 3 cycle, 0.16µm, 25p
4% PFA RT 60 min, 0.1% NaBH4, 10µm section, 3% NDS, 0.3% Triton, 60min RT Block, 1:1000 Pri Dil 12 hr, 1:1000 Sec Dil 60min, No Postfix, No Postfix Quench, 20U Glu. Ox. 71.5mM BME, 100U Catalase, 20mM MEA, 200nm Step size,250f, 3 cycle, 0.16µm, 25p
4% PFA RT 60 min, 0.5% NaBH4, 10µm section, 3% NDS, 0.3% Triton, 60min RT Block, 1:1000 Pri Dil 12 hr, 1:1000 Sec Dil 60min, No Postfix, No Postfix Quench, 20U Glu. Ox. 71.5mM BME, 100U Catalase, 20mM MEA, 200nm Step size,250f, 3 cycle, 0.16µm, 25p
4% PFA RT 60 min, No Quench, 10um section, 3% NDS, 0.3% Triton, 60min RT Block, 1:1000 Pri Dil 12 hr, 1:1000 Sec Dil 60min, No Postfix, No Postfix Quench, 20U Glu. Ox. 71.5mM BME, 100U Catalase, 20mM MEA, 200nm Step size,250f, 3 cycle, 0.16µm, 25p
4% PFA RT 60 min, No Quench, 20um section, 3% NDS, 0.3% Triton, 60min RT Block, 1:1000 Pri Dil 12 hr, 1:1000 Sec Dil 60min, No Postfix, No Postfix Quench, 20U Glu. Ox. 71.5mM BME, 100U Catalase, 20mM MEA, 200nm Step size,250f, 3 cycle, 0.16µm, 25p
4% PFA RT 60 min, No Quench, 10µm section, 1% NDS, 0.3% Triton, 60min RT Block, 1:1000 Pri Dil 12 hr, 1:1000 Sec Dil 60min, No Postfix, No Postfix Quench, 20U Glu. Ox. 71.5mM BME, 100U Catalase, 20mM MEA, 200nm Step size,250f, 3 cycle, 0.16µm, 25p
4% PFA RT 60 min, No Quench, 10µm section, 2% NDS, 0.3% Triton, 60min RT Block, 1:1000 Pri Dil 12 hr, 1:1000 Sec Dil 60min, No Postfix, No Postfix Quench, 20U Glu. Ox. 71.5mM BME, 100U Catalase, 20mM MEA, 200nm Step size,250f, 3 cycle, 0.16µm, 25p
4% PFA RT 60 min, No Quench, 10µm section, 5% NDS, 0.3% Triton, 60min RT Block, 1:1000 Pri Dil 12 hr, 1:1000 Sec Dil 60min, No Postfix, No Postfix Quench, 20U Glu. Ox. 71.5mM BME, 100U Catalase, 20mM MEA, 200nm Step size,250f, 3 cycle, 0.16µm, 25p
4% PFA RT 60 min, No Quench, 10µm section, 10% NDS, 0.3% Triton, 60min RT Block, 1:1000 Pri Dil 12 hr, 1:1000 Sec Dil 60min, No Postfix, No Postfix Quench, 20U Glu. Ox. 71.5mM BME, 100U Catalase, 20mM MEA, 200nm Step size,250f, 3 cycle, 0.16µm, 25p
4% PFA RT 60 min, No Quench, 10µm section, 15% NDS, 0.3% Triton, 60min RT Block, 1:1000 Pri Dil 12 hr, 1:1000 Sec Dil 60min, No Postfix, No Postfix Quench, 20U Glu. Ox. 71.5mM BME, 100U Catalase, 20mM MEA, 200nm Step size,250f, 3 cycle, 0.16µm, 25p
4% PFA RT 60 min, No Quench, 10µm section, 3% NDS, 0.1% Triton, 60min RT Block, 1:1000 Pri Dil 12 hr, 1:1000 Sec Dil 60min, No Postfix, No Postfix Quench, 20U Glu. Ox. 71.5mM BME, 100U Catalase, 20mM MEA, 200nm Step size,250f, 3 cycle, 0.16µm, 25p
4% PFA RT 60 min, No Quench, 10µm section, 3% NDS, 0.3% Triton, 60min RT Block, 1:1000 Pri Dil 12 hr, 1:1000 Sec Dil 60min, No Postfix, No Postfix Quench, 20U Glu. Ox. 71.5mM BME, 100U Catalase, 20mM MEA, 200nm Step size,250f, 3 cycle, 0.16µm, 25p
4% PFA RT 60 min, No Quench, 10µm section, 3% NDS, 0.5% Triton, 60min RT Block, 1:1000 Pri Dil 12 hr, 1:1000 Sec Dil 60min, No Postfix, No Postfix Quench, 20U Glu. Ox. 71.5mM BME, 100U Catalase, 20mM MEA, 200nm Step size,250f, 3 cycle, 0.16µm, 25p
4% PFA RT 60 min, No Quench, 10µm section, 3% NDS, 1.0% Triton, 60min RT Block, 1:1000 Pri Dil 12 hr, 1:1000 Sec Dil 60min, No Postfix, No Postfix Quench, 20U Glu. Ox. 71.5mM BME, 100U Catalase, 20mM MEA, 200nm Step size,250f, 3 cycle, 0.16µm, 25p
4% PFA RT 60 min, No Quench, 10µm section, 3% NDS, 2.0% Triton, 60min RT Block, 1:1000 Pri Dil 12 hr, 1:1000 Sec Dil 60min, No Postfix, No Postfix Quench, 20U Glu. Ox. 71.5mM BME, 100U Catalase, 20mM MEA, 200nm Step size,250f, 3 cycle, 0.16µm, 25p
4% PFA RT 60 min, No Quench, 10µm section, 3% NDS, 0.1% Saponin, 60min RT Block, 1:1000 Pri Dil 12 hr, 1:1000 Sec Dil 60min, No Postfix, No Postfix Quench, 20U Glu. Ox. 71.5mM BME, 100U Catalase, 20mM MEA, 200nm Step size,250f, 3 cycle, 0.16µm, 25p
4% PFA RT 60 min, No Quench, 10µm section, 3% NDS, 0.3% Saponin, 60min RT Block, 1:1000 Pri Dil 12 hr, 1:1000 Sec Dil 60min, No Postfix, No Postfix Quench, 20U Glu. Ox. 71.5mM BME, 100U Catalase, 20mM MEA, 200nm Step size,250f, 3 cycle, 0.16µm, 25p
4% PFA RT 60 min, No Quench, 10µm section, 3% NDS, 0.5% Saponin, 60min RT Block, 1:1000 Pri Dil 12 hr, 1:1000 Sec Dil 60min, No Postfix, No Postfix Quench, 20U Glu. Ox. 71.5mM BME, 100U Catalase, 20mM MEA, 200nm Step size,250f, 3 cycle, 0.16µm, 25p
4% PFA RT 60 min, No Quench, 10µm section, 3% NDS, 1.0% Saponin, 60min RT Block, 1:1000 Pri Dil 12 hr, 1:1000 Sec Dil 60min, No Postfix, No Postfix Quench, 20U Glu. Ox. 71.5mM BME, 100U Catalase, 20mM MEA, 200nm Step size,250f, 3 cycle, 0.16µm, 25p
4% PFA RT 60 min, No Quench, 10µm section, 3% NDS, 2.0% Saponin, 60min RT Block, 1:1000 Pri Dil 12 hr, 1:1000 Sec Dil 60min, No Postfix, No Postfix Quench, 20U Glu. Ox. 71.5mM BME, 100U Catalase, 20mM MEA, 200nm Step size,250f, 3 cycle, 0.16µm, 25p
4% PFA RT 60 min, No Quench, 10µm section, 3% NDS, 0.3% Triton, No Block, 1:1000 Pri Dil 12 hr, 1:1000 Sec Dil 60min, No Postfix, No Postfix Quench, 20U Glu. Ox. 71.5mM BME, 100U Catalase, 20mM MEA, 200nm Step size,250f, 3 cycle, 0.16µm, 25p
4% PFA RT 60 min, No Quench, 10µm section, 3% NDS, 0.3% Triton, 4C 30 min Block, 1:1000 Pri Dil 12 hr, 1:1000 Sec Dil 60min, No Postfix, No Postfix Quench, 20U Glu. Ox. 71.5mM BME, 100U Catalase, 20mM MEA, 200nm Step size,250f, 3 cycle, 0.16µm, 25p
4% PFA RT 60 min, No Quench, 10µm section, 3% NDS, 0.3% Triton, 4C 120 min Block, 1:1000 Pri Dil 12 hr, 1:1000 Sec Dil 60min, No Postfix, No Postfix Quench, 20U Glu. Ox. 71.5mM BME, 100U Catalase, 20mM MEA, 200nm Step size,250f, 3 cycle, 0.16µm, 25p
4% PFA RT 60 min, No Quench, 10µm section, 3% NDS, 0.3% Triton, RT 30 min Block, 1:1000 Pri Dil 12 hr, 1:1000 Sec Dil 60min, No Postfix, No Postfix Quench, 20U Glu. Ox. 71.5mM BME, 100U Catalase, 20mM MEA, 200nm Step size,250f, 3 cycle, 0.16µm, 25p
4% PFA RT 60 min, No Quench, 10µm section, 3% NDS, 0.3% Triton, RT 120 min Block, 1:1000 Pri Dil 12 hr, 1:1000 Sec Dil 60min, No Postfix, No Postfix Quench, 20U Glu. Ox. 71.5mM BME, 100U Catalase, 20mM MEA, 200nm Step size,250f, 3 cycle, 0.16µm, 25p

4% PFA RT 60 min, No Quench, 10µm section, 3% NDS, 0.3% Triton, 60min RT Block, 1:1000 Pri Dil 12 hr, 1:100 Sec Dil 60min, No Postfix, No Postfix Quench, 20U Glu. Ox. 71.5mM BME, 100U Catalase, 20mM MEA, 200nm Step size,250f, 3 cycle, 0.16µm, 25p
4% PFA RT 60 min, No Quench, 10µm section, 3% NDS, 0.3% Triton, 60min RT Block, 1:1000 Pri Dil 12 hr, 1:1000 Sec Dil 60min, No Postfix, No Postfix Quench, 20U Glu. Ox. 71.5mM BME, 100U Catalase, 20mM MEA, 200nm Step size,250f, 3 cycle, 0.16µm, 25p
4% PFA RT 60 min, No Quench, 10µm section, 3% NDS, 0.3% Triton, 60min RT Block, 1:1000 Pri Dil 12 hr, 1:5000 Sec Dil 60min, No Postfix, No Postfix Quench, 20U Glu. Ox. 71.5mM BME, 100U Catalase, 20mM MEA, 200nm Step size,250f, 3 cycle, 0.16µm, 25p
4% PFA RT 60 min, No Quench, 10µm section, 3% NDS, 0.3% Triton, 60min RT Block, 1:1000 Pri Dil 12 hr, 1:100 Sec Dil 60min, No Postfix, No Postfix Quench, 20U Glu. Ox. 71.5mM BME, 100U Catalase, 20mM MEA, 200nm Step size,250f, 3 cycle, 0.16µm, 25p
4% PFA RT 60 min, No Quench, 10µm section, 3% NDS, 0.3% Triton, 60min RT Block, 1:1000 Pri Dil 12 hr, 1:1000 Sec Dil 60min, No Postfix, No Postfix Quench, 20U Glu. Ox. 71.5mM BME, 100U Catalase, 20mM MEA, 200nm Step size,250f, 3 cycle, 0.16µm, 25p
4% PFA RT 60 min, No Quench, 10µm section, 3% NDS, 0.3% Triton, 60min RT Block, 1:1000 Pri Dil 12 hr, 1:5000 Sec Dil 60min, No Postfix, No Postfix Quench, 20U Glu. Ox. 71.5mM BME, 100U Catalase, 20mM MEA, 200nm Step size,250f, 3 cycle, 0.16µm, 25p
4% PFA RT 60 min, No Quench, 10µm section, 3% NDS, 0.3% Triton, 60min RT Block, 1:1000 Pri Dil 12 hr, 1:1000 Sec Dil 60min, 1% PFA 10 min Postfix, No Postfix Quench, 20U Glu. Ox. 71.5mM BME, 100U Catalase, 20mM MEA, 200nm Step size,250f, 3 cycle, 0.16µm, 25p
4% PFA RT 60 min, No Quench, 10µm section, 3% NDS, 0.3% Triton, 60min RT Block, 1:1000 Pri Dil 12 hr, 1:1000 Sec Dil 60min, 2% PFA 10 min Postfix, No Postfix Quench, 20U Glu. Ox. 71.5mM BME, 100U Catalase, 20mM MEA, 200nm Step size,250f, 3 cycle, 0.16µm, 25p
4% PFA RT 60 min, No Quench, 10µm section, 3% NDS, 0.3% Triton, 60min RT Block, 1:1000 Pri Dil 12 hr, 1:1000 Sec Dil 60min, 4% PFA 10 min Postfix, No Postfix Quench, 20U Glu. Ox. 71.5mM BME, 100U Catalase, 20mM MEA, 200nm Step size,250f, 3 cycle, 0.16µm, 25p
4% PFA RT 60 min, No Quench, 10µm section, 3% NDS, 0.3% Triton, 60min RT Block, 1:1000 Pri Dil 12 hr, 1:1000 Sec Dil 60min, 1% PFA 30 min Postfix, No Postfix Quench, 20U Glu. Ox. 71.5mM BME, 100U Catalase, 20mM MEA, 200nm Step size,250f, 3 cycle, 0.16µm, 25p
4% PFA RT 60 min, No Quench, 10µm section, 3% NDS, 0.3% Triton, 60min RT Block, 1:1000 Pri Dil 12 hr, 1:1000 Sec Dil 60min, 2% PFA 30 min Postfix, No Postfix Quench, 20U Glu. Ox. 71.5mM BME, 100U Catalase, 20mM MEA, 200nm Step size,250f, 3 cycle, 0.16µm, 25p
4% PFA RT 60 min, No Quench, 10µm section, 3% NDS, 0.3% Triton, 60min RT Block, 1:1000 Pri Dil 12 hr, 1:1000 Sec Dil 60min, 4% PFA 30 min Postfix, No Postfix Quench, 20U Glu. Ox. 71.5mM BME, 100U Catalase, 20mM MEA, 200nm Step size,250f, 3 cycle, 0.16µm, 25p
4% PFA RT 60 min, No Quench, 10µm section, 3% NDS, 0.3% Triton, 60min RT Block, 1:1000 Pri Dil 12 hr, 1:1000 Sec Dil 60min, No Postfix, 10mM Glycine Postfix Quench, 20U Glu. Ox. 71.5mM BME, 100U Catalase, 20mM MEA, 200nm Step size,250f, 3 cycle, 0.16µm, 25p
4% PFA RT 60 min, No Quench, 10µm section, 3% NDS, 0.3% Triton, 60min RT Block, 1:1000 Pri Dil 12 hr, 1:1000 Sec Dil 60min, No Postfix, 100mM Glycine Postfix Quench, 20U Glu. Ox. 71.5mM BME, 100U Catalase, 20mM MEA, 200nm Step size,250f, 3 cycle, 0.16µm, 25p
4% PFA RT 60 min, No Quench, 10µm section, 3% NDS, 0.3% Triton, 60min RT Block, 1:1000 Pri Dil 12 hr, 1:1000 Sec Dil 60min, No Postfix, 10mM NH3Cl Postfix Quench, 20U Glu. Ox. 71.5mM BME, 100U Catalase, 20mM MEA, 200nm Step size,250f, 3 cycle, 0.16µm, 25p
4% PFA RT 60 min, No Quench, 10µm section, 3% NDS, 0.3% Triton, 60min RT Block, 1:1000 Pri Dil 12 hr, 1:1000 Sec Dil 60min, No Postfix, 100mM NH3Cl Postfix Quench, 20U Glu. Ox. 71.5mM BME, 100U Catalase, 20mM MEA, 200nm Step size,250f, 3 cycle, 0.16µm, 25p
4% PFA RT 60 min, No Quench, 10µm section, 3% NDS, 0.3% Triton, 60min RT Block, 1:1000 Pri Dil 12 hr, 1:1000 Sec Dil 60min, No Postfix, No Postfix Quench, 20U Glu. Ox. 0mM BME, 100U Catalase, 20mM MEA, 200nm Step size,250f, 3 cycle, 0.16µm, 25p
4% PFA RT 60 min, No Quench, 10µm section, 3% NDS, 0.3% Triton, 60min RT Block, 1:1000 Pri Dil 12 hr, 1:1000 Sec Dil 60min, No Postfix, No Postfix Quench, 20U Glu. Ox. 71.5mM BME, 100U Catalase, 20mM MEA, 200nm Step size,250f, 3 cycle, 0.16µm, 25p
4% PFA RT 60 min, No Quench, 10µm section, 3% NDS, 0.3% Triton, 60min RT Block, 1:1000 Pri Dil 12 hr, 1:1000 Sec Dil 60min, No Postfix, No Postfix Quench, 20U Glu. Ox. 143mM BME, 100U Catalase, 20mM MEA, 200nm Step size,250f, 3 cycle, 0.16µm, 25p
4% PFA RT 60 min, No Quench, 10µm section, 3% NDS, 0.3% Triton, 60min RT Block, 1:1000 Pri Dil 12 hr, 1:1000 Sec Dil 60min, No Postfix, No Postfix Quench, 20U Glu. Ox. 286mM BME, 100U Catalase, 20mM MEA, 200nm Step size,250f, 3 cycle, 0.16µm, 25p
4% PFA RT 60 min, No Quench, 10µm section, 3% NDS, 0.3% Triton, 60min RT Block, 1:1000 Pri Dil 12 hr, 1:1000 Sec Dil 60min, No Postfix, No Postfix Quench, 20U Glu. Ox. 71.5mM BME, 0U Catalase, 20mM MEA, 200nm Step size,250f, 3 cycle, 0.16µm, 25p
4% PFA RT 60 min, No Quench, 10µm section, 3% NDS, 0.3% Triton, 60min RT Block, 1:1000 Pri Dil 12 hr, 1:1000 Sec Dil 60min, No Postfix, No Postfix Quench, 20U Glu. Ox. 71.5mM BME, 20U Catalase, 20mM MEA, 200nm Step size,250f, 3 cycle, 0.16µm, 25p
4% PFA RT 60 min, No Quench, 10µm section, 3% NDS, 0.3% Triton, 60min RT Block, 1:1000 Pri Dil 12 hr, 1:1000 Sec Dil 60min, No Postfix, No Postfix Quench, 20U Glu. Ox. 71.5mM BME, 100U Catalase, 20mM MEA, 200nm Step size,250f, 3 cycle, 0.16µm, 25p
4% PFA RT 60 min, No Quench, 10µm section, 3% NDS, 0.3% Triton, 60min RT Block, 1:1000 Pri Dil 12 hr, 1:1000 Sec Dil 60min, No Postfix, No Postfix Quench, 20U Glu. Ox. 71.5mM BME, 500U Catalase, 20mM MEA, 200nm Step size,250f, 3 cycle, 0.16µm, 25p
4% PFA RT 60 min, No Quench, 10µm section, 3% NDS, 0.3% Triton, 60min RT Block, 1:1000 Pri Dil 12 hr, 1:1000 Sec Dil 60min, No Postfix, No Postfix Quench, 0U Glu. Ox. 71.5mM BME, 100U Catalase, 20mM MEA, 200nm Step size,250f, 3 cycle, 0.16µm, 25p
4% PFA RT 60 min, No Quench, 10µm section, 3% NDS, 0.3% Triton, 60min RT Block, 1:1000 Pri Dil 12 hr, 1:1000 Sec Dil 60min, No Postfix, No Postfix Quench, 10U Glu. Ox. 71.5mM BME, 100U Catalase, 20mM MEA, 200nm Step size,250f, 3 cycle, 0.16µm, 25p
4% PFA RT 60 min, No Quench, 10µm section, 3% NDS, 0.3% Triton, 60min RT Block, 1:1000 Pri Dil 12 hr, 1:1000 Sec Dil 60min, No Postfix, No Postfix Quench, 200U Glu. Ox. 71.5mM BME, 100U Catalase, 20mM MEA, 200nm Step size,250f, 3 cycle, 0.16µm, 25p
4% PFA RT 60 min, No Quench, 10µm section, 3% NDS, 0.3% Triton, 60min RT Block, 1:1000 Pri Dil 12 hr, 1:1000 Sec Dil 60min, No Postfix, No Postfix Quench, 40U Glu. Ox. 71.5mM BME, 100U Catalase, 20mM MEA, 200nm Step size,250f, 3 cycle, 0.16µm, 25p
4% PFA RT 60 min, No Quench, 10µm section, 3% NDS, 0.3% Triton, 60min RT Block, 1:1000 Pri Dil 12 hr, 1:1000 Sec Dil 60min, No Postfix, No Postfix Quench, 20U Glu. Ox. 71.5mM BME, 100U Catalase, 0mM MEA, 200nm Step size,250f, 3 cycle, 0.16µm, 25p
4% PFA RT 60 min, No Quench, 10µm section, 3% NDS, 0.3% Triton, 60min RT Block, 1:1000 Pri Dil 12 hr, 1:1000 Sec Dil 60min, No Postfix, No Postfix Quench, 20U Glu. Ox. 71.5mM BME, 100U Catalase, 10mM MEA, 200nm Step size,250f, 3 cycle, 0.16µm, 25p
4% PFA RT 60 min, No Quench, 10µm section, 3% NDS, 0.3% Triton, 60min RT Block, 1:1000 Pri Dil 12 hr, 1:1000 Sec Dil 60min, No Postfix, No Postfix Quench, 20U Glu. Ox. 71.5mM BME, 100U Catalase, 20mM MEA, 200nm Step size,250f, 3 cycle, 0.16µm, 25p
4% PFA RT 60 min, No Quench, 10µm section, 3% NDS, 0.3% Triton, 60min RT Block, 1:1

Supplemental Table 2: Primary antibodies used

Antigen	Labeling specificity	Source	Dilution (confocal)	Dilution (RAIN-STORM)
Calbindin D-28K	Horizontal cells, subsets of amacrine cells, and retinal ganglion cells	Swant, Cat# CB38a, RRID: AB_10000340	1:5000	1:1000
CD31	Blood vessels, endothelial cells	Fisher, Cat# BDB5500274, RRID: AB_393571	1:200	1:50
Cone arrestin	Cone photoreceptors	Millipore, Cat# AB15282, RRID: AB_11210270	1:2000	1:1000
Collagen IV	Blood vessels	Millipore, Cat# AB769, RRID: AB_92262	1:1000	1:500
Connexin 43	Pericyte gap junctions	Sigma, Cat#C6219, RRID: AB_476857	1:1000	1:500
Desmin	Pericytes	Thermo Fisher, Cat# MA513259, RRID: AB_11000611	1:500	1:500
Dystrophin	Photoreceptor synapses	Abcam, Cat# ab15277, RRID: AB_301813	1:200	1:100
Glutamine synthetase (GS)	Muller glia	BD Biosciences, Cat# 610517, RRID: AB_397879	1:1000	1:500
GFAP	Astrocytes	Sigma, Cat# G3893, RRID: AB_477010	1:500	1:500
Iba1	Microglia	Abcam, Cat# ab5076, RRID: AB_2224402	1:500	1:500
Islet1	ON bipolar cells, starburst amacrine cells, subset of retinal ganglion cells	R&D system, Cat# AF1837, RRID: AB_2126324	1:2000	1:1000
NG2	Pericytes	Abcam, Cat# ab129051, RRID: AB_2877152	1:1000	1:500
PKCα	Rod bipolar cells	Abcam, Cat# ab31, RRID: AB_303507	1:500	1:500
PSD95	Photoreceptor terminals	Abcam, Cat# ab12093, RRID: AB_298846	1:500	1:500
RIBEYE	Ribbon synapses	Synaptic system, Cat#192103, RRID: AB_2086775	1:500	1:500
Secretagogin (SCGN)	Cone bipolar cells	BioVendor, Cat# RD181120100, RRID: AB_2034060	1:1000	1:500
Tau	Microtubule-associated protein	Proteintech, Cat#66499-1-Ig, RRID: AB_2881863	1:1000	1:500
α-Tubulin	α-Tubulin protein	Sigma, Cat#T5168-.2ML, RRID: AB_477579	1:1000	1:500
Tomm20	Mitochondria	Abcam, Cat# ab78547, RRID: AB_2043078	1:1000	1:500
Tyrosine hydroxylase (TH)	Dopaminergic amacrine cell subset	EMD Millipore, Cat# AB1542, RRID: AB_90755	1:2000	1:500
Vesicular glutamate transporter 1 (VGlut1)	Photoreceptor ribbon synapses	Abcam, Cat# ab77822, RRID: AB_2187677	1:500	1:250
Vesicular glutamate transporter 3 (VGlut3)	Subset of amacrine cells	Millipore, Cat#AB5421, RRID: AB_2187832	1:1000	1:500